ADVANCING EARTH AND SPACE SCIENCES

JGR Space Physics

RESEARCH ARTICLE
10.1029/2025JA034732

The Contribution of the Russell-McPherron Effect to the Semiannual Variation in Thermospheric Density

Mike Lockwood[1], **Chris J. Scott**[1], **James O'Donoghue**[1], **Mat J. Owens**[1], and **Luke A. Barnard**[1]

[1]Department of Meteorology, University of Reading, Reading, UK

Key Points:

- The Russell-McPherron effect is identified by the effect of the Y-component polarity of the interplanetary magnetic field in the GSEQ frame
- This provides insight of the role of geomagnetic activity in modulating global mean thermospheric densities
- When the IMF Y-component in GSEQ exceeds 4 nT the R-M effect drives over half of the semiannual variation in global mean thermospheric density

Correspondence to:
M. Lockwood,
m.lockwood@reading.ac.uk

Citation:
Lockwood, M., Scott, C. J., O'Donoghue, J., Owens, M. J., & Barnard, L. A. (2026). The contribution of the Russell-McPherron effect to the semiannual variation in thermospheric density. *Journal of Geophysical Research: Space Physics*, *131*, e2025JA034732. https://doi.org/10.1029/2025JA034732

Received 4 OCT 2025
Accepted 6 MAY 2026

Author Contributions:
Conceptualization: Mike Lockwood, James O'Donoghue, Mat J. Owens
Data curation: Luke A. Barnard
Formal analysis: Mike Lockwood
Funding acquisition: Chris J. Scott, James O'Donoghue, Mat J. Owens
Investigation: Mike Lockwood
Methodology: Mike Lockwood, Chris J. Scott, James O'Donoghue
Project administration: Mike Lockwood, Mat J. Owens
Resources: Chris J. Scott, Mat J. Owens
Software: Mike Lockwood, Luke A. Barnard
Validation: Mike Lockwood, Chris J. Scott, James O'Donoghue, Mat J. Owens, Luke A. Barnard
Visualization: Mike Lockwood, James O'Donoghue, Mat J. Owens, Luke A. Barnard
Writing – original draft: Mike Lockwood

Abstract A number of external sources and internal circulation mechanisms have been proposed to explain the well-known semiannual variation in global mean thermospheric densities. We use the polarity of the Y-component (dawn to dusk) of the Interplanetary Magnetic Field (IMF) in the Geocentric Solar Equatorial (GSEQ) frame to identify the influence, via geomagnetic currents, of the Russell-McPherron (R-M) effect on solar wind-to-magnetosphere energy coupling. Using data from 1996 to 2025, our best estimate is that for an IMF $|[B_Y]_{GSEQ}|$ component of magnitude 4 nT or greater, more than half of the semiannual variation in global averages of thermospheric density at altitudes between 460 km and 530 km is externally driven by the R-M effect and the associated geomagnetic activity and that other effects that do not depend on the IMF Y-component, such as the "spoon" mechanism or upward energy transport from below by waves and tides, are responsible for the remainder. For all data, including quieter geomagnetic conditions, our best estimate is that the R-M mechanism contributes 20% of the semiannual variation of thermospheric densities.

Plain Language Summary The mass density of gas in Earth's upper atmosphere is important as it controls the orbital speed and altitude of spacecraft and space junk and can cause them to re-enter and burn up in the lower atmosphere. Since soon after the start of the space age, it has been known from changes to the orbits of satellites that the global average of this density has a semiannual variation with peaks near the two equinoxes. This was generally ascribed to upward heat transfer from the lower atmospheric layers or an internal circulation known as the "spoon" mechanism, but this paper shows that a significant driver for this semiannual variation is also ionospheric currents driven by the solar wind passing by earth's magnetic field, which can drive more than half of the semiannual variation.

1. Introduction

1.1. The Russell-McPherron Effect

The Russell-McPherron effect (Russell & McPherron, 1973) (hereafter, the "R-M effect") is demonstrated by Figure 1 and, for reasons outlined later in this section, is known to be the dominant effect controlling the time-of-day and time-of-year pattern of average (i.e., averaged over all solar activity levels) power extraction from the solar wind by Earth's coupled magnetosphere-ionosphere-thermosphere system. However, there are a number of common misconceptions about this mechanism and its effects that we address here. The R-M effect influences the average pattern of power extraction because it is systematic; however, it is only very rarely the dominant effect driving large space weather events. The key element controlling solar wind energy extraction by Earth's magnetosphere is the (southward) component of the Interplanetary Magnetic Field (IMF) anti-parallel to the Earth's magnetic axis $\vec{\mathbf{M}}$, usually quantified by a negative Z-component in the Geocentric Solar Magnetospheric (GSM) reference frame, $[B_Z]_{GSM}$ (see Figure 1). Lockwood et al. (2016) and Lockwood, McWilliams, et al. (2020) show that the dominant influence on this southward IMF in GSM $\left([B_Z]_{GSM} < 0\right)$ during major terrestrial space-weather events is southward IMF in a solar frame (such as the Geocentric Solar Ecliptic, GSE, or Geocentric Solar Equatorial, GSEQ, frames) and that in major events, the R-M effect contributes only a very small fraction to the total negative $[B_Z]_{GSM}$, compared to the effect of negative $[B_Z]_{GSEQ}$. This is demonstrated by Figure 2 for the data set used in the present paper (from between 1 January 1996 and 1 April 2025). These plots are for 1-min resolution IMF data that has been averaged into 3-hr bins to match the *am* geomagnetic activity index: *am* is derived from the range of variation in observations of Earth's field by a network of mid-latitude observatories in 3-hr intervals (Mayaud, 1980). The IMF data are obtained from the Omni data set which gives the IMF components in the GSE and GSM frames, estimated from in situ satellite observations (mainly from spacecraft in

Writing – review & editing: Mike Lockwood, Chris J. Scott, James O'Donoghue, Mat J. Owens, Luke A. Barnard

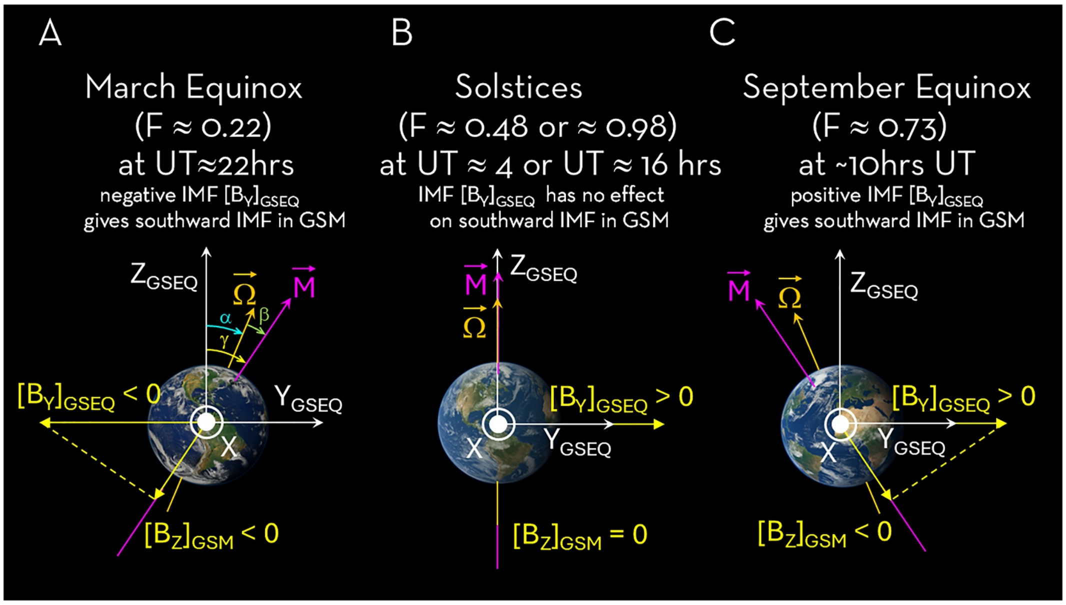

Figure 1. An explanation of the Russell-McPherron (R-M) effect using three views of Earth from the Sun at some selected fractions of the calendar year (F) and Universal times (UT). Values of F and UT given are approximate and for the present day and do vary on centennial timescales with the variations in Earth's orbital parameters. The GSEQ reference frame is the most relevant to the structure of the Interplanetary Magnetic Field (IMF) whereas the IMF in the GSM frame is most relevant to energy coupling into the magnetosphere. The X axis of both frames points from the center of the Earth to the center of the Sun. In the GSEQ frame, the Y axis lies parallel to the solar equator and the IMF Y component and is positive from dawn to dusk. Z_{GSEQ} makes up the right hand set. In GSM, the Y and Z axes are rotated around the X axis until the Z axis is aligned with the projection of Earth's magnetic axis $\vec{\mathbf{M}}$ onto the YZ plane: $\vec{\mathbf{M}}$ makes an angle β with the rotation axis $\vec{\mathbf{\Omega}}$ and so precesses around $\vec{\mathbf{\Omega}}$ with Earth's daily rotation. $\vec{\mathbf{\Omega}}$ makes an angle α with the Z_{GSEQ} axis and precesses around it with Earth's orbit around the Sun. Part (a) is for the time when the angle between the Z_{GSEQ} axis and the projection of $\vec{\mathbf{M}}$ onto the YZ plane, γ (defined here as positive toward dusk) is a maximum of $(\beta + \alpha)$ which happens near 22 hrs UT about 2 weeks after the March equinox: then large negative IMF $[B_Y]_{GSEQ}$ yields geoeffective southward IMF, $[B_Z]_{GSM} < 0$, as shown. Part (c) is for 10 hrs UT and about 2 weeks after the September equinox, when γ is a minimum value of -$(\beta + \alpha)$: at this time it is large positive IMF $[B_Y]_{GSEQ}$ that yields geoeffective southward IMF, $[B_Z]_{GSM} < 0$. Part (b) shows one out of a number of times when $\gamma = 0$ and the $[B_Y]_{GSEQ}$ component is perpendicular to Z_{GSM} and so has no effect on $[B_Z]_{GSM}$. Note that this will not only occur when the projection of $\vec{\mathbf{\Omega}}$ onto the YZ plane aligned with Z_{GSEQ} (as shown in Part c): this is because the projection of $\vec{\mathbf{M}}$ can still align with Z_{GSEQ} at times close enough to the solstices to make the angle between the projection of $\vec{\mathbf{\Omega}}$ and Z_{GSEQ} small enough.

orbit around the L1 Lagrange point) for the time of impact on the nose of the magnetosphere. The GSEQ components are computed at one-minute resolution from the GSE components, using the rotation angle between the two frames which, due to the 7.25° inclination of the ecliptic to the solar equatorial plane, varies with F—the fraction of time in a calendar year that has elapsed in that year—over the range ±7.25°. The $[B_Z]_{GSM}$ values and $[B_Z]_{GSEQ}$ values are here averaged into the 3-hr intervals over which *am* geomagnetic index values are compiled, brought forward by an hour to make allowance for the average one-hour response time of the *am* index, which is the mean of the distribution of values for a full range of F- Universal Time (UT) bins and *am* activity levels, revealed by Figure 9 of Lockwood, McWilliams, et al. (2020). The panels in Figure 2 show the logarithm of the numbers of these three-hourly IMF component means, color-coded and in bins that are 0.2 nT by 0.2 nT in size, as a function of the Z-component values in the GSM frame (vertical axis) and in the GSEQ frame (horizontal axis). The data cluster around the mauve line where $[B_Z]_{GSM} = [B_Z]_{GSEQ}$ and the broadening of the distribution about that line shows the effect of the R-M mechanism. Part a of Figure 2 is for all data, but the other panels select the data by the (lagged) *am* value exceeding a given quantile of its distribution: parts b–d are, respectively, for the top 10%, 5% and 1% of all *am* values in the interval. It can be seen that as the geomagnetic activity level increases, the IMF is in increasingly in the negative $[B_Z]_{GSM}$ and negative $[B_Z]_{GSEQ}$ sector.

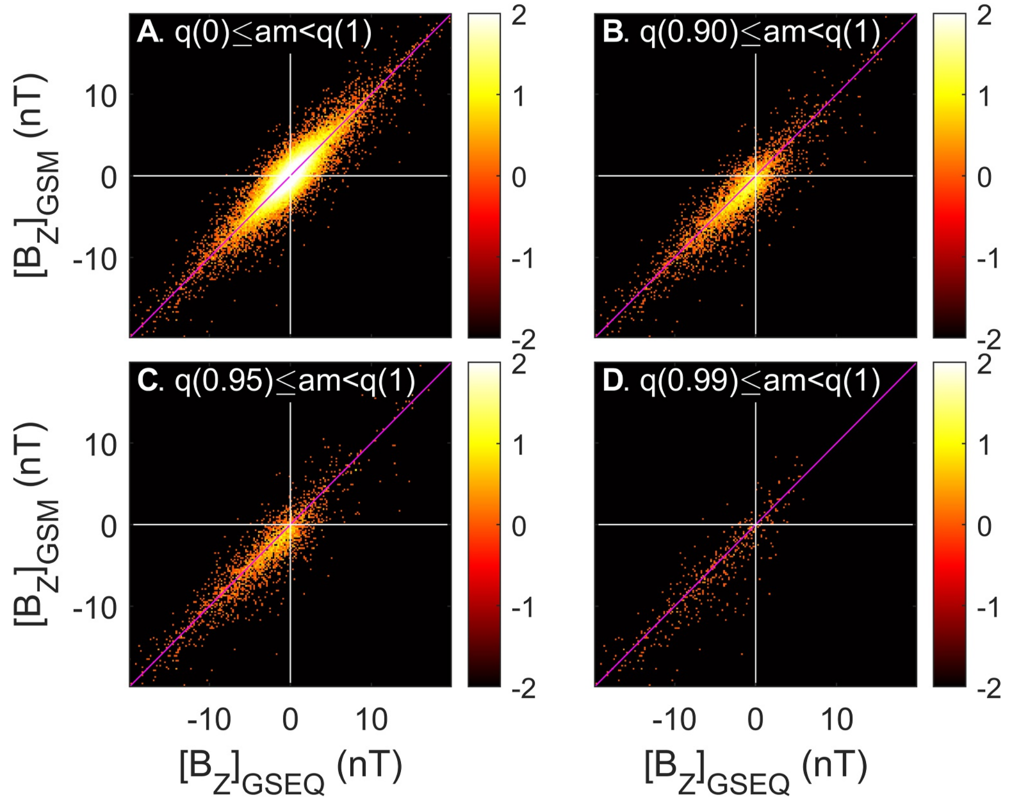

Figure 2. The relationship between the southward IMF component in the GSEQ and GSM frames, demonstrated for the data used in this paper (for the interval 1 January 1996–1 April 2025). The logarithm of the number of 3-hourly means, $\log_{10}(N)$, is color-coded in bins of size 0.2 nT by 0.2 nT as function of the IMF Z-component in the GSM and GSEQ frames. The mauve line is at $[B_Z]_{GSM} = [B_Z]_{GSEQ}$. One-minute resolution Omni data are used that have been averaged into the 3-hr bins used to compile the *am* index values, shifted forward in time by a 1-hr response lag. Part (a) is for all data. Part (b) is for top 10% of *am* values ($q(0.9)$ is the upper decile of the distribution of *am* values), part (c) is for the top 5% and (d) for the top 1%. This is an updated version of Figure 1 of the paper by Lockwood, McWilliams, et al. (2020).

Figure 2 demonstrates that large geomagnetic disturbances, driven by large negative $[B_Z]_{GSM}$, are primarily caused by events with large negative $[B_Z]_{GSEQ}$ hitting Earth's magnetosphere. The R-M effect does still play a minor role because the favored/unfavored polarity field in the Y direction for a given equinox does, in general, add to/detract from the negative GSM Z component, giving data points, respectively, above and below the mauve lines in Figure 2. However, this contribution is relatively small. Nevertheless, the R-M effect does still contribute to F-UT pattern in the numbers of large storms (as well as to the pattern for mean values), as shown by Figure 12 of Lockwood, Owens, Barnard, Haines, et al. (2020), even though it does not make the largest contribution to $[B_Z]_{GSM}$ in most cases. This contribution of the R-M effect can be seen in Figure 2d because, for the largest *am* events, more data points are below the mauve line than above it, giving an average value of $\left(|[B_Z]_{GSM}| - |[B_Z]_{GSEQ}|\right)$; in the $[B_Z]_{GSM} < 0$ and $[B_Z]_{GSEQ} < 0$ quadrant of 1.1 nT hence the R-M effect in these events of high geomagnetic activity is adding to the southward field more often than it is detracting from it. If we take data for all levels of geomagnetic activity, as in Figure 2a, this effect is still present but the asymmetry in this quadrant is diluted by the quiet magnetic activity intervals, giving an average $\left(|[B_Z]_{GSM}| - |[B_Z]_{GSEQ}|\right)$ of 0.2 nT.

The R-M effect is the conversion of IMF Y-component in the GSEQ frame into Z-component in the GSM frame by the orientation of Earth's magnetic axis, $\vec{\mathbf{M}}$. This is significant because $[B_Y]_{GSEQ}$ is often, but certainly not always, the dominant component in the YZ plane of that frame. As demonstrated by Figure 2, events of large southward field in GSM, occur mainly because of events of large southward field in GSEQ, and these are often caused by transient events in the heliosphere, such as Interplanetary Coronal Mass Ejections (ICMEs). The incidence of such events on Earth, in terms of time-of-day (Universal Time, UT) and time-of year (fraction of a

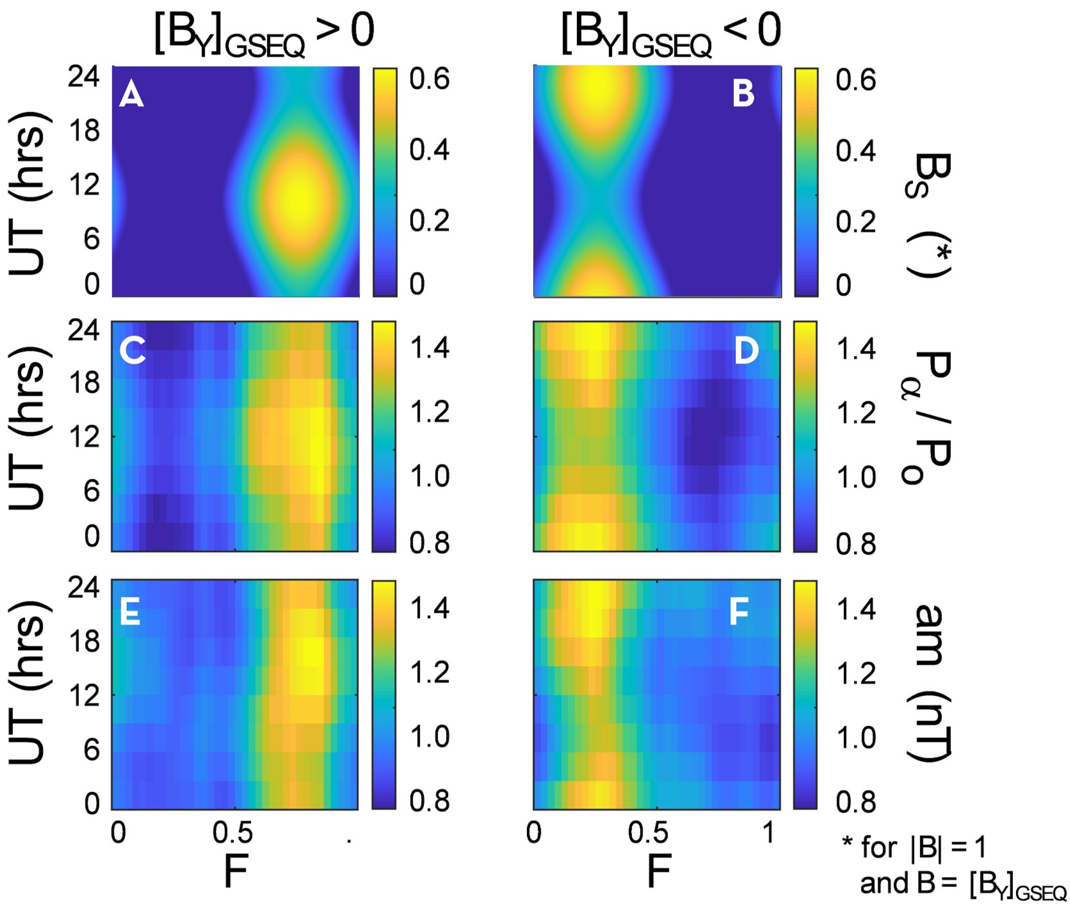

Figure 3. Demonstration of the R-M effect on the *am* geomagnetic index for the data set used in this paper using *F*-*UT* plots where *F* is the fraction of a calendar year and *UT* is the Universal time (in fact, the modern variant, *UTC*, is used). The left hand column (parts a, c, and e) is for IMF $[B_Y]_{GSEQ} > 0$ and the right-hand column (parts b, d and f) for $[B_Y]_{GSEQ} < 0$. Parts (a) and (b) show the idealized R-M effect, color coding the geoeffective southward IMF component in the GSM frame B_S (given by Equation 1 for an idealized IMF of that points in the $\pm Y$ direction and has unity magnitude) in bins that are $dF = (1/365)$ wide in F and $dUT = 0.1$ hr wide in UT. For each bin, the angle γ shown in Figure 1 is computed from ephemeris data. Parts (c–f) are made from observations and use bins that are $dF = 1/36$ wide in F and $dUT = 3$ hr wide in UT. Parts (c) and (d) show the estimated power input into the magnetosphere, P_α (normalized to its overall mean value, P_o), computed from one-minute solar wind and IMF data using the formula given by Vasyliunas et al. (1982) (Equation 3). Parts (e) and (f) show the *F*-*UT* patterns for the *am* geomagnetic index. This is a collection of updated versions of figure panels presented by Lockwood, Owens, Barnard, Haines, et al. (2020).

calender year, *F*) is essentially random. Hence their effect, although much larger than that of the R-M effect, is averaged out and shows systematic variations with neither *UT* nor *F*. Note, however, that the incidence of large transients is the cause of the systematic solar-cycle variation in events of large solar wind energy extraction by the magnetosphere because such events are considerably more common at sunspot maximum (Lamy et al., 2019; Scolini et al., 2018; Webb & Howard, 1994).

A complication is that we do not see the characteristic R-M response pattern when a geomagnetic activity index is plotted as a function of *UT* and *F*, although we do see the strong semiannual variation in *F* inherent in the R-M pattern if we average over all *UT* at a given *F* (Cliver et al., 2000; Lockwood, Owens, Barnard, Haines, et al., 2020). As explained by Figure 1 (and as shown in the top row of Figure 3) the characteristic R-M pattern has peaks near 22 hrs *UT* about 2 weeks after the March equinox and near 10 hrs *UT* about 2 weeks after the September equinox. Instead of the R-M pattern, for indices that respond primarily to the ring current, such as the *Dst* index, we see an "axial pattern" with a strong semiannual variation but no variation with *UT*. This is often ascribed to the original explanation by Cortie (1912), invoking the effect of Earth's annual variation in heliographic latitude, Λ_H (between $-7.25°$ and $+7.25°$) and the variation in average solar wind speed with Λ_H (called the "axial effect"). However, that consistent latitudinal variation in solar wind speed is only present at solar minimum and, even then, is not large, given that the Earth only moves 7.25^o away from the heliographic equator, resulting in an average solar wind speed variation of just $\sim 10\%$. Lockwood et al. (2016) show that this axial pattern is actually not inconsistent with the R-M effect if the index is either averaged, or has an inherent smoothing response, with a timescale of about 12 hr or greater, which is the case for ring current indices such as *Dst*.

Before discussing *F-UT* patterns in geomagnetic activity any further, we need to place a caveat that a suitable geomagnetic activity index must be employed. Specifically, we require one that has a very constant response to solar wind drivers (with both *F* and *UT*) and at all activity levels. This eliminates indices that do not monitor both hemispheres in matching ways: the effect of solar radiation on ionospheric conductivities will strongly enhance the causal currents in the summer hemisphere and so lead to a non-solar wind variations with *F*. Similarly, the index needs to be constructed from as uniform a distribution of stations in longitude as possible or spurious *UT* variations will be introduced. Lockwood, Chambodut, et al. (2019) have studied the response of mid-latitude geomagnetic indices and show that because the *kp* (and hence *ap*) indices are made from a network of stations with a very uneven geographic distribution, and because of the way data are mapped back to a single calibration station, they imprint a strong *F-UT* pattern on the data and so are not suitable for such pattern studies. On the other hand, the *am* index (Mayaud, 1980) is compiled from data taken by rings of stations in both hemispheres that are as evenly-spaced in longitude as is possible (and uses weighting functions to reduce the effect of inhomogeneities in the rings caused by extensive oceans, particularly in the southern hemisphere). As a result, *am* has an exceptionally flat response as a function with both *F* and *UT* and so is ideal for studies of *F-UT* patterns resulting from external drivers (Lockwood, Chambodut, et al., 2019). The *Dst* index is also good as it is compiled using equatorial stations so the annual variation effect of dipole tilt is reduced: however, *Dst* uses only 4 such stations and the large gaps in longitude give an inhomogeneous response in *UT*. More recently, a *Dst*-like index called *Dcx* has been developed at the University of Oulu (Karinen & Mursula, 2005). This employs 19 stations (in definitive form) or 15 stations (in preliminary form) over a larger range of latitudes and so has a much more even response. Mursula and Karinen (2005) argue that this avoids an excessively large semiannual response that is seen in *Dst*.

The complication is that the *am* geomagnetic index shows a semiannual variation with a systematic *UT* variation that gives an hourglass-like pattern called the "McIntosh" or "equinoctial" pattern (Bartels, 1925; Chambodut et al., 2013; Cliver et al., 2000; De La Sayette & Berthelier, 1996; Lockwood, Owens, Barnard, Haines, et al., 2020; McIntosh, 1959): this pattern is considerably different from the R-M *F-UT* pattern and, as first pointed out by Bartels (1925), is associated with the effect of Earth's dipole tilt toward or away from the Sun (in the *XZ* plane), in addition to the angle γ in the *YZ* plane (see Figure 1) that the R-M effect allows for. This dipole tilt varies with *F* because of the rotation axis of the Earth $\vec{\mathbf{\Omega}}$ is fixed in direction with respect to the stars (on the timescales that we are interested in here) and Earth orbits around the Sun (the same effect as gives us the seasons). It also varies with *UT* because Earth's magnetic axis $\vec{\mathbf{M}}$ precesses around $\vec{\mathbf{\Omega}}$ with the rotation of the Earth. This tilt of Earth's magnetic axis toward or away from the Sun is not part of the R-M effect and so some models of solar wind-magnetosphere coupling have tried to modify the R-M effect in attempts to include this tilt effect and thereby reproduce the observed equinoctial pattern. However, this neglects the fact that geomagnetic activity is not only influenced by the energy extracted from the solar wind flow but is also modulated by the storage and release of energy in the geomagnetic tail of the magnetosphere. Lockwood, McWilliams, et al. (2020), Lockwood, Owens, Barnard, Watt, et al. (2020), and Lockwood, Owens, Barnard, Haines, et al. (2020) have provided evidence that this dipole tilt influences the internal storage-release system through its effect on the "hinge point" in the tail that separates the inner geomagnetic field (i.e., oriented with respect to $\vec{\mathbf{M}}$) and the far tail (i.e., oriented by the solar wind flow into a direction close to antisunward, i.e., close to the $-X$ direction). The angle of this hinge varies with the dipole tilt angle and its effect on the storage-release system in the mid-tail of the magnetosphere was first suggested by Kivelson and Hughes (1990). Lockwood, McWilliams, et al. (2020) and Lockwood, Owens, Barnard, Watt, et al. (2020) provide evidence that this internal magnetospheric effect is the origin of the equinoctial pattern in geomagnetic activity because they show that the amplitude of that pattern depends strongly on the solar wind dynamic pressure, P_{SW} and this is a separate influence from the power input into the magnetosphere. This is because P_{SW} squeezes the mid-tail and so also modulates the storage and release of magnetic energy there. Evidence that the energy stored in the tail depends on P_{SW} has long been available (Caan et al., 1973). Furthermore, increases in P_{SW} have been shown to initiate the release mechanisms, causing the onset of substorm expansion phases (Kokubun et al., 1977; Schieldge & Siscoe, 1970; C. Yue et al., 2010) and, conversely, Karlsson et al. (2000) showed that a sudden decrease in P_{SW} can cause the energy release in a substorm expansion to fizzle out. Lockwood, McWilliams, et al. (2020) showed that the amplitude of the equinoctial pattern increased linearly with P_{SW}. In addition, Finch et al. (2008) showed that the geomagnetic response to P_{SW} was predominantly in region of the nightside substorm current wedge and (Lockwood, 2013; Lockwood et al., 2021) showed that the equinoctial F-UT pattern in geomagnetic activity was strongest for stations in the midnight Magnetic Local Time (MLT) sector and weakest for those in the noon MLT sector. This supports the idea that the equinoctial pattern is associated with processes in the geomagnetic tail, rather that with solar-wind magnetospheric coupling. Modeling (Lockwood, Owens, Barnard, Watt, et al., 2020) also supports this idea that the R-M mechanism and pattern controls the average power input into the magnetosphere but the equinoctial pattern arises from the internal magnetospheric storage and release system that controls the deposition of that power into the ionosphere and thermosphere.

One method to distinguish R-M, axial and equinoctial mechanisms—which was proposed by Russell and McPherron (1973)—is that the equinox peaks are at slightly different F for the three mechanisms; however, in practice, for the numbers of data points available to us since the start of the space age, we cannot reliably resolve these small differences in the times of the peaks (Lockwood, Owens, Barnard, Haines, et al., 2020). Nevertheless, there is one test that leaves no doubt that the R-M effect is the cause of the semiannual variation in average power input into the magnetosphere. This was used by Zhao and Zong (2012) and Lockwood, McWilliams, et al. (2020) and relies on the fact that the R-M effect is unique in predicting that positive values of the Y component of IMF (roughly dawn to dusk) in the GSEQ frame, $[B_Y]_{GSEQ}$, will cause the September peak of the semiannual variation and that $[B_Y]_{GSEQ} < 0$ will cause the March peak, as demonstrated by Figure 1. These authors clearly show that sorting the data by negative/positive IMF $[B_Y]_{GSEQ}$ gives the March/September equinox peak. This is a unique prediction of the R-M effect and the amplitude of the peaks shows it is the major factor in the average power extraction from the solar wind. Lockwood, McWilliams, et al. (2020) showed the March and September peaks of the equinoctial pattern required, respectively, negative and positive $[B_Y]_{GSEQ}$, proving that the modulation of energy extraction by the R-M effect was at the core of the equinoctial pattern, even if the R-M pattern could not explain the S-like shape of the equinox peaks.

The original paper by Russell and McPherron (1973) used a half-wave rectified southward IMF B_S to describe solar wind magnetosphere coupling, defined by

$$\begin{gathered} B_S = -[B_Z]_{GSM} \; for \quad [B_Z]_{GSM} < 0 \\ and \\ B_S = 0 \; for \quad [B_Z]_{GSM} > 0 \end{gathered} \tag{1}$$

However B_S is discontinuous in slope at $[B_Z]_{GSM} = 0$ and does not allow for continued, but small and tapering, energy input into the magnetosphere as the IMF turns increasingly northward in GSM. Finch and Lockwood (2007) and Lockwood and McWilliams (2021) find that B_S performs significantly less well in coupling functions that predict energy input into the magnetosphere and geomagnetic activity and that much better is the geoeffective IMF formulation:

$$B_G = B_{YZ} \times \sin^4(\theta_{GSM}/2) \tag{2}$$

Where $B_{YZ} = \left([B_Y]_{GSM}^2 + [B_Z]_{GSM}^2\right)^{1/2}$ is the magnitude of the IMF vector projected onto the ZY plane. The angle θ_{GSM} is the "clock angle" that the vector $\overrightarrow{\mathbf{B_{YZ}}}$ makes with the Z (northward) axis of the GSM frame: $\theta_{GSM} = \tan^{-1}\left(\left|[B_Y]_{GSM}\right|/[B_Z]_{GSM}\right)$ is derived for a given IMF orientation, F and UT using the angle γ shown in Figure 1 to orient the GSM frame.

The difference between the half-wave rectified form B_S, as defined by Equation 1, and the effective form B_G, defined by Equation 2 has implications for the R-M effect which are discussed in Appendix B of the paper by Lockwood, Owens, Barnard, Haines, et al. (2020).

We here use a more sophisticated coupling function that makes use of the IMF orientation term in Equation 2, but allows for solar speed (V_{SW}) and number density (N_{SW}), as well as the IMF and its orientation, as proposed by

Vasyliunas et al. (1982). This is based analytically on the power density in the solar wind which is dominated by the kinetic energy of the solar wind particles, and not the Poynting flux as has often been assumed. (Note that Lockwood (2019) has investigated adding a small analytic correction that allows for the contribution of a few percent made by Poynting flux, but that is not employed here). The formulation of Vasyliunas et al. (1982) is

$$P_\alpha = K \times B^{2\alpha} \times (N_{SW} m_{SW})^{2/3-\alpha} \times V_{SW}^{7/3-2\alpha} \times \sin^4(\theta_{GSM}/2) \quad (3)$$

where K is a collection of constants, which can be calculated from Equation 8 of the paper by Lockwood (2019) to give an absolute value of P_α but here is canceled by normalizing P_α by its overall average for the whole data set. In this equation, m_{SW} is the mean solar wind ion mass and α is the one free fit parameter: this arises from the unknown dependence on the solar wind Mach number, and the value giving the best correlation with terrestrial activity metrics depends on the metric used and the timescale over which the data are averaged. Studies show that values of α in the range 0.35–0.45 provide very good prediction of geomagnetic activity indices (Lockwood, 2019; Lockwood et al., 2019a, 2019b).

Figure 3 illustrates how effective the IMF $[B_Y]_{GSEQ}$ polarity test is at evaluating the influence of the R-M effect, by studying its control of the *am* geomagnetic index and of the power estimated to enter the magnetosphere using the coupling function of Vasyliunas et al. (1982). The top row of Figure 3 uses the idealized R-M model, as employed by Russell and McPherron (1973) in their original paper, in which the IMF at Earth lies in a plane parallel to the heliographic equator and here has a Y-component in GSEQ of unity magnitude ($[B_Z]_{GSEQ} = 0$ and $[B_Y]_{GSEQ} = \pm 1$). Like the original R-M paper, it uses the half wave rectified southward field B_S.

The panels of the second row contrast the idealized model patterns shown in the top row by showing the *F-UT* variation of the power input P_α (here normalized to its overall average value P_o) into the magnetosphere, computed from solar wind and IMF data using Equation 3 and which has shown to correlate best with the *am* index at all timescales (Finch & Lockwood, 2007; Lockwood & McWilliams, 2021; Lockwood et al., 2019a). This formulation employs the $\sin^4(\theta_{GSM}/2)$ IMF orientation factor used by B_G and we here employ a coupling exponent of $\alpha = 0.44$ which Lockwood et al. (2019b) showed gives the optimum prediction of the 3-hourly *am* data. The R-M pattern is clearly seen. However careful inspection reveals a small but important difference between the top and second rows of Figure 3: the original R-M patterns predicted in the top row show the maxima but, elsewhere, there is a constant background (of zero) because of the half-wave rectification inherent in B_S. The patterns for P_α/P_o clearly show the same peaks but away from those peaks there are distinct minima (at the F and UT of the peak for the opposite polarity of $[B_Y]_{GSEQ}$). These minima are of magnitude $P_\alpha/P_o \approx 0.8$ whereas the maxima are of magnitude $P_\alpha/P_o \approx 1.5$: hence the minima are smaller in magnitude than the peaks and so they do not fully cancel the maxima if the pattern is generated for all data and not sorted by $[B_Y]_{GSEQ}$ polarity; however, they do reduce the amplitude of the pattern for both polarities. Hence the full amplitude of the R-M pattern is only seen when it is separated into the two polarities and B_G (or equivalents) is used rather than B_S. The bottom row of Figure 3 shows the response of the *am* geomagnetic index. The same patterns are seen in *am* as in P_α/P_o, although some of the "S-shape" of the equinoctial pattern is becoming evident and peaks are at slightly greater UT, due to the response lag of *am*.

The key point about all three rows of Figure 3 is that sorting the data by the polarity of the IMF Y-component in the GSEQ coordinate frame causes complete separation of the March and the September equinox peaks, as is uniquely predicted by the R-M mechanism. From this, we know that the R-M effect does control the average energy transfer from the solar wind into the magnetosphere and the subsequent average response of the magnetosphere-ionosphere current systems that determine the *am* geomagnetic index.

1.2. The Semiannual Variation in Thermospheric Densities

Annual and semiannual oscillations in globally-averaged thermospheric densities were first observed by Paetzold and Zschörner (1961) using satellite drag data. More recent reviews of these oscillations have been given by Emmert (2015), Jones et al. (2018) and J. Yue et al. (2019). Thermospheric density variations are driven by a number of influences. A large factor is solar extreme ultraviolet (EUV) irradiance, which is the primary source of heating for the thermosphere which expands and contracts with, respectively, increased and decreased EUV flux: the density at a given altitude increases or decreases as a result. Other sources of heating are: Joule heating by the ionospheric currents that are detected on the ground by magnetometers ("geomagnetic activity") (Wang et al., 2020); energetic particles precipitating from the magnetosphere (Wilson et al., 2006); and waves and tides originating in the lower atmosphere that propagate upward into the thermosphere (Forbes et al., 2017; Yiğit et al., 2021). The geomagnetic heating is much stronger during geomagnetic storms (Wang et al., 2021) and has time-dependent effects on the altitude profile of thermospheric density (Huang et al., 2012). It can be quantified for the ionospheric E-region currents associated with the large-scale pattern of F-region plasma convection (Weimer, 2005) but also has contributions associated with mesoscale current eddies (Meng et al., 2022).

In the present paper, we study the semiannual variation in global averages of thermospheric densities, but we note that this variation is detected at all latitudes (J. Guo et al., 2010) and is linked to differences between the north and south hemispheres (Lei et al., 2012; Qian et al., 2023; Qian & Solomon, 2012). Fuller-Rowell (1998) proposed that a large-scale inter-hemispheric circulation was the cause of the global semiannual density variation. In this mechanism, the large-scale circulation acts as a "spoon" to mix the atmosphere and, because it is stronger during solstice seasons when there is greater hemispheric difference, this mechanism ultimately causes the global semiannual variation in neutral density with maxima during equinox seasons and minima during solstices (Jones et al., 2018). Note that this mechanism is largely internal to Earth's atmosphere.

The focus of the current paper is the contribution to the semiannual variation in global thermospheric densities that is made by the R-M effect. Previous studies have estimated this to be small compared with the other effects (Detman, 1996) and, in particular, some modeling studies suggest that the spoon effect dominates (Jones et al., 2018). However, we note that some other modeling studies find that the spoon mechanism is insufficient to explain the semiannual variation: using the Thermosphere-Ionosphere-Electrodynamics General Circulation Model (TIE-GCM), Qian et al. (2009) needed to add seasonally-varying eddy diffusion, representing contributions from the lower atmospheric forcing, at the lower boundary (at an altitude of 97 km) of the model to bring the simulated mass density into good agreement with satellite drag data. Bowman et al. (2008) studied the semiannual variation by analyzing satellite drag data from 28 satellites at altitudes throughout the thermosphere for the interval 1969–2006. They showed that the semiannual variation varied in amplitude from year to year, with peak variability at around 800 km altitude. They found the solar activity dependence of the amplitude variability to be weak around 400 km, but the amplitude increased with solar activity at greater altitudes. Emmert and Picone (2010) presented a climatological analysis of daily globally averaged density data, at heights between 200 and 600 km for the interval 1967–2007. They found that the amplitudes of annual and semiannual variations of thermospheric density only slightly increased with increased solar activity.

In the present paper we use the same test for the influence on thermospheric densities of the R-M effect based on IMF $[B_Y]_{GSEQ}$ that was used to evaluate the semiannual variation in geomagnetic activity by Zhao and Zong (2012), Lockwood, Owens, Barnard, Haines, et al. (2020), and Lockwood, McWilliams, et al. (2020). We note that D. Guo et al. (2015) have, effectively, already applied this test by sorting the thermospheric data by the sector structure: we apply it here at higher time resolution by sorting according to daily values of the IMF $[B_Y]_{GSEQ}$ component.

This paper needs to consider a number of complications. In Section 2 we describe the data used. In Section 3.1 we explain the need to introduce thresholds to apply the best test for the R-M effect on the semi-annual variation in thermospheric densities and describes two ways to implement them. In Section 3.2 we describe the method to remove the annual variation. In Section 3.3 we use an example threshold to demonstrate the quantification of the R-M effect. Section 3.4 explains the need to evaluate the effect of the threshold. Section 3.5 points out a potential coupling of annual and semiannual effects of EUV heating of the thermosphere. Section 3.6 presents a sensitivity study of the effects of varying the thresholds. Section 3.7 studies why the March peak of the semiannual variation in thermospheric densities is generally larger than the September peak. Finally, Section 4 presents a summary discussion of the results and the conclusions of the paper.

2. Data Employed

We use two sources of thermospheric densities derived from satellite orbit data to cover as long an interval as possible and also to provide a check on each. The SWARM satellites provide data from 2014 to the present. In that time, SWARM-A and SWARM-C operated at altitudes 465 km and 480 km, while SWARM-B was between 510 km and 520 km. The derivation of the thermospheric densities from the orbits and accelerometers on board is

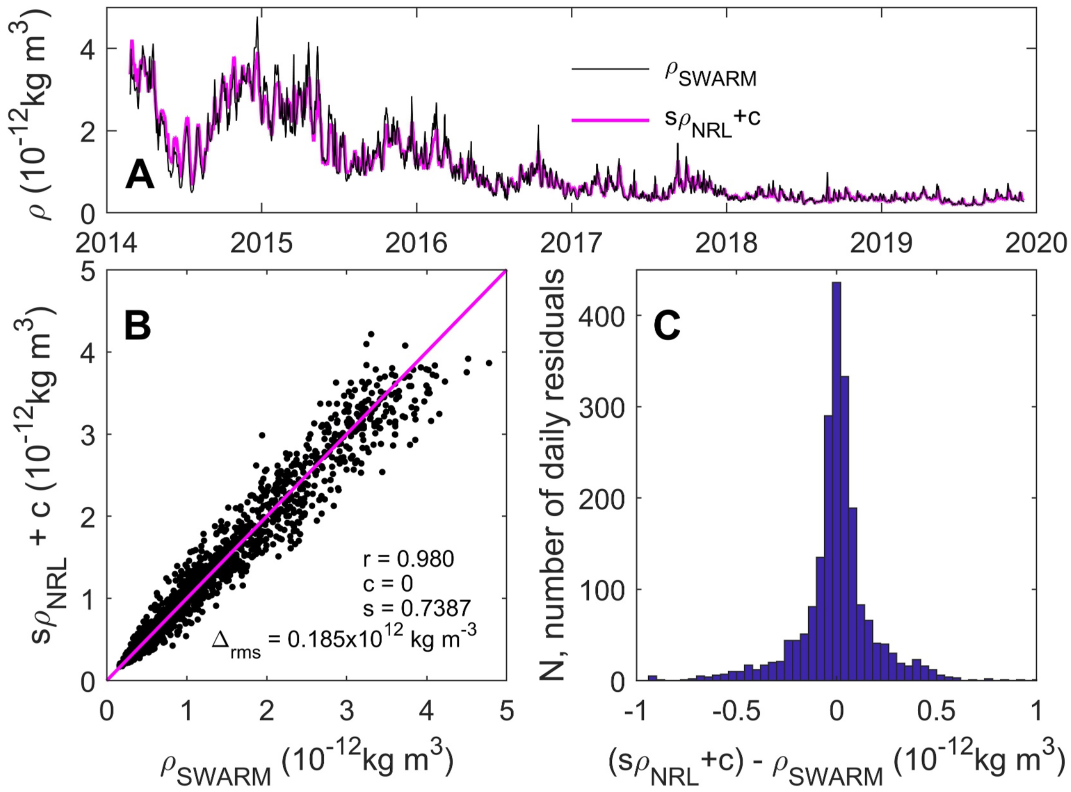

Figure 4. Inter-calibration of the daily SWARM and NRL estimates of global mean thermospheric mass density, ρ. (a) The time series for the overlap interval (2014–2020). The average of the three SWARM data series (from SWARM-A, -B and -C), ρ_{SWARM} is given in black and values from the NRL data set, linear regressed to the ρ_{SWARM} values, in mauve. The best-fit linear regression, $s \times \rho_{NRL} + c$ has slope $s = 0.738$ and intercept $c = 0$. (The non unity value of s allows for the altitude difference between the best-fit NRL and SWARM data). These data are compared in a scatter plot in part (b) and have a linear correlation coefficient of $r = 0.983$. Part (c) shows the distribution of fit residuals that have a root mean square value of Δ_{rms} of 0.1849×10^{-12} kg m^{-3}.

described by Doornbos (2012) and Siemes et al. (2016) and the data processed and made available by T.U. Delft in the Netherlands. We here average all available data from all 3 SWARM craft. The Naval Research Laboratory (NRL) data on thermospheric densities are derived from the orbit data of over 7,700 spacecraft (and other orbiting objects) and are given for altitudes of [250 : 25 : 575] km for 1967–2019 (inclusive), as described by Emmert et al. (2021). These data are made available by the Naval Research Laboratory, Washington, DC, USA. The high degree of agreement between these data set is demonstrated by Figure 4 which is for the overlap period on 2014–2020.

The NRL data series for altitude $h = 400$ km is used as this gives the highest correlation coefficient ($r = 0.983$) and the lowest fit residual Δ_{rms} of 0.1849×10^{-12} kg m^{-3}. This is a slightly lower altitude than that from where the SWARM data were taken and so the best-fit linear regression has a of slope $s = 0.738$ and an intercept $c = 0$. That the correlation is best for a slightly lower h in the NRL data than for the SWARM data reflects the difference in processing of the two data series. The inter-calibration of the two data sets shown in Figure 4 yields the splined data series shown part a of Figure 5 for 1 January 1996–1 April 2025, which is the interval for which we have 1-min data on the interplanetary magnetic field.

The other panels in Figure 5 show the other daily means used in this study. Part b shows the mid-latitude *am* index (Lockwood, Chambodut, et al., 2019; Mayaud, 1980). Part c shows the *Dcx* index that largely responds to ring current enhancements and is increasingly negative with increasing activity (Karinen & Mursula, 2005; Mursula & Karinen, 2005).

Parts d and e are based on one-minute values of the $[B_Y]_{GSEQ}$ component of the IMF. These are obtained from the components of the IMF in the GSE (Geocentric Solar Ecliptic) frame given by NASA's Omniweb data service,

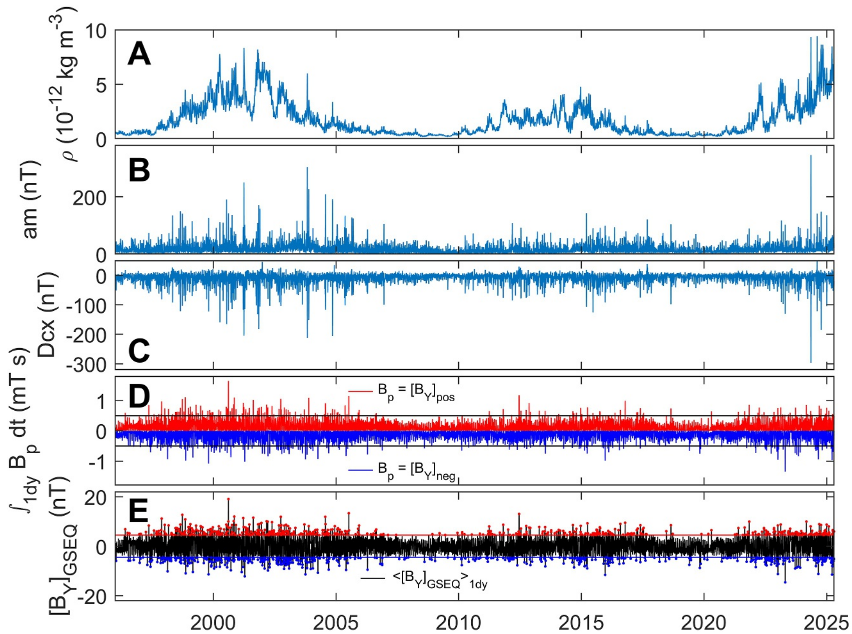

Figure 5. The variations of daily means of parameters used in this paper for 1 January 1996–1 April 2025. (a) The series of thermospheric density, ρ, splined from the SWARM and NRL data as described by Figure 4. (b) The *am* mid-latitude geomagnetic index. (c) The *Dcx* low-latitude geomagnetic index. (d) The integrated Y-component of the IMF in the GSEQ frame of a given polarity over each day, $\int_{1dy} B_p\ dt$ where B_p is the one-minute averages of $[B_Y]_{GSEQ}$ of that polarity: red is for $[B_Y]_{GSEQ} > 0$ and blue for $[B_Y]_{GSEQ} < 0$. The black horizontal lines are at $\pm 0.5 \times 10^{-3}\ T\ s$. (e) Daily mean values of the IMF Y-component in GSEQ, $\langle [B_Y]_{GSEQ} \rangle_{1dy}$: values above the threshold of +4.5 nT (the red line) are marked with red dot and values below (more negative than) the threshold of −4.5 nT (the blue line) are marked with a blue dot.

transformed into the GSEQ frame. These values are available from 1 January 1996 onward. Panel d sorts the 1 min values in $[B_Y]_{GSEQ}$ each day into values of one polarity (generically called B_p here for both sets of values) and integrates them. The red and blue panels show the integrals over the day of, respectively, the positive and negative values $\left(\int_{1dy} B_p\ dt\right)$. The black lines are at $\pm 0.5 \times 10^{-3}\ T\ s$, a threshold which usually defines which polarity is dominant in a day, but we note can be exceeded for both polarities of B_p if the IMF field strength is large and the IMF orientation variable. Part e shows the daily mean values of $[B_Y]_{GSEQ}$, $\langle [B_Y]_{GSEQ} \rangle_{1dy}$. The red and blue lines mark thresholds of +4.5 nT and −4.5 nT which are used (in the next section) to define days that are predominantly $[B_Y]_{GSEQ} > 0$ (the points given by red dots) or predominantly $[B_Y]_{GSEQ} < 0$ (the points given by blue dots). Again we note that days that are predominantly of one polarity (giving a mean of that polarity) can, and in general will, contain intervals of the opposite polarity.

In the next Section, we sort all the data series shown in Figure 5 in two ways. Firstly we sort into two categories using the mean daily mean values shown in part e with $\langle [B_Y]_{GSEQ} \rangle_{1dy} > +4.5$ nT and $\langle [B_Y]_{GSEQ} \rangle_{1dy} < -4.5$ nT. Secondly we use $\int_{1dy} [B_p]_{GSEQ} dt > 0.5 \times 10^{-3}\ T\ s$ and $\int_{1dy} [B_p]_{GSEQ} dt < -0.5 \times 10^{-3}\ T\ s$. These are the thresholds shown in Figure 5. We carried out sensitivity studies to look at the effects of varying these thresholds, which will be discussed later in this paper (Section 3.6). In general, lower thresholds yield lower-differences between the two equinox peaks. This is not surprising as the periods of the non-dominant (minority) polarity of $[B_Y]_{GSEQ}$ in a day become more important and this raises the minority equinox peak and so reduces the difference between the two equinox peaks. This problem arises because we only have global thermospheric density data with time resolution of a day and variability of the IMF orientation on minute timescales is sufficiently great for much of the time, that intervals of both the dominant and non-dominant $[B_Y]_{GSEQ}$ polarity occur within each day. Thus variability in the polarity of the IMF $[B_Y]_{GSEQ}$ component within the day dilutes the detection of the R-M effect from the difference in the amplitudes of the two equinox peaks. The thresholds illustrated in Figure 5 are compromises, being big enough to ensure a clear difference between the two peaks but not so large that a high degree of noise is introduced into the semi-annual variation by small numbers of samples in the time-of-year bins. These thresholds are sufficient to show that the R-M effect is indeed present in the data and to illustrate the method used. In Section 3.6, we carry out a sensitivity study to see how the effect varies with the threshold adopted.

We sort each of the daily parameters (thermospheric densities and geomagnetic indices) using the above selections of the IMF $[B_Y]_{GSEQ}$ component in the same day. For the all the terrestrial data sets, the separation of the semiannual variations for the two categories of IMF $[B_Y]_{GSEQ}$ was reduced if we introduced a lag of one or more days.

3. Results

3.1. Semiannual Variations

Figure 6 shows the thermospheric and geomagnetic variations with fraction of a calendar year, F. Mean values are taken in 20 bins of F (which are 18.25 days wide for non leap years and 18.3 days wide for leap years). The number 20 is a compromise—it yields 10 bins to define each peak in the semiannual variation (which is adequate as we are not concerned with the precise timing of the peaks) but is not too large which would introduce statistical noise because of the lower sample numbers. The red lines are for days with positive IMF $[B_Y]_{GSEQ}$ (above the adopted threshold, T) and the blue lines are for negative $[B_Y]_{GSEQ}$ (with values below $-T$). The left hand plots use the daily means $\langle [B_Y]_{GSEQ} \rangle_{1dy}$ to define the "majority polarity" of $[B_Y]_{GSEQ}$ for that day. With each day there may (probably will) have been intervals with IMF of the opposite $[B_Y]_{GSEQ}$ polarity to the dominant polarity for the day. This 'minority polarity' field will enhance the other equinox to that enhanced by the majority polarity field and so act to reduce the March/September peak difference detected. This effect of the minority population of $[B_Y]_{GSEQ}$ values within a given day can be identified in the September data as small increases in geomagnetic activity for $[B_Y]_{GSEQ} < 0$ (blue lines): this is seen in Part b of Figure 6 for the *am* index as a small peak close to the equinox and in Part d for the *Dcx* index as a small minimum at the same time. However, this cannot be identified in the March equinox data for $[B_Y]_{GSEQ} > 0$, presumably because the minority $[B_Y]_{GSEQ}$ polarity data happen to be less concentrated at the equinox as for the September equinox.

To try to reduce this effect of the minority $[B_Y]_{GSEQ}$ polarity in a day, we also use the integrated polarities and sort into $\int_{1dy} B_p dt > +0.5 \times 10^{-3}\ T\ s$ and $\int_{1dy} B_p dt < -0.5 \times 10^{-3}\ T\ s$, this gives the variations with F shown in the right hand plots of Figure 6 that are similar to those in the left hand plots. However, we note that the right-hand plots e and f, which sort by $\int_{1dy} B_p dt$, do not show the small September activity peaks for the unfavored polarity that are present in the left-hand plots b and c and so we conclude the effect of minority polarity field in the day is indeed reduced by this second method of sorting the data (shown in the right hand column of the figure).

The lower two rows of Figure 6 show that using both the mean and integrated $[B_Y]_{GSEQ}$ criteria give peak geomagnetic activity at the September/March equinox (in both *am* and *Dcx*) for majority-positive and majority-negative $[B_Y]_{GSEQ}$ days, respectively. As pointed out by Zhao and Zong (2012) and Lockwood, McWilliams, et al. (2020), this is an unique prediction of the R-M mechanism. The interesting point, in the context of the present paper, is that the same effect is seen in thermospheric densities, ρ, in Parts a and d of Figure 6—albeit with a small difference between the two IMF $[B_Y]_{GSEQ}$ polarity peaks than for the geomagnetic data.

This section demonstrates that the R-M effect is contributing the semiannual variation in thermospheric densities. However, in Parts a and d of Figure 6 show peaks for both red and blue lines at both equinoxes. This means there are peaks for both the polarities (the "favored" and the "unfavored" polarity for the R-M effect at a given equinox). This is also true for the geomagnetic indices *am* and $-Dcx$ in parts b and c, but the unfavored polarity peaks are weaker but there are no detectable unfavored polarity peaks in parts e or f. Because in all panels the favored polarity peak exceeds the unfavored polarity peak, the R-M effect is present; however, because the unfavored polarity in part c gives peaks at both equinoxes for thermospheric density, whereas none is seen in parts e or f, we conclude there is a second mechanism enhancing thermospheric densities at the equinoxes in addition to the R-M effect, whereas the R-M effect is sufficient on its own to explain the equinox peaks in *am* and $-Dcx$. Hence, the R-M effect is enhancing the semiannual effect but is not wholly responsible for it. However, we need to remain aware that intervals of the minority polarity $[B_Y]_{GSEQ}$ within each day will also contribute to these lesser peaks at the unfavored equinox. This is therefore remains a complication when we try to evaluate the relative contributions of the R-M effect and the combined effect of all other mechanisms.

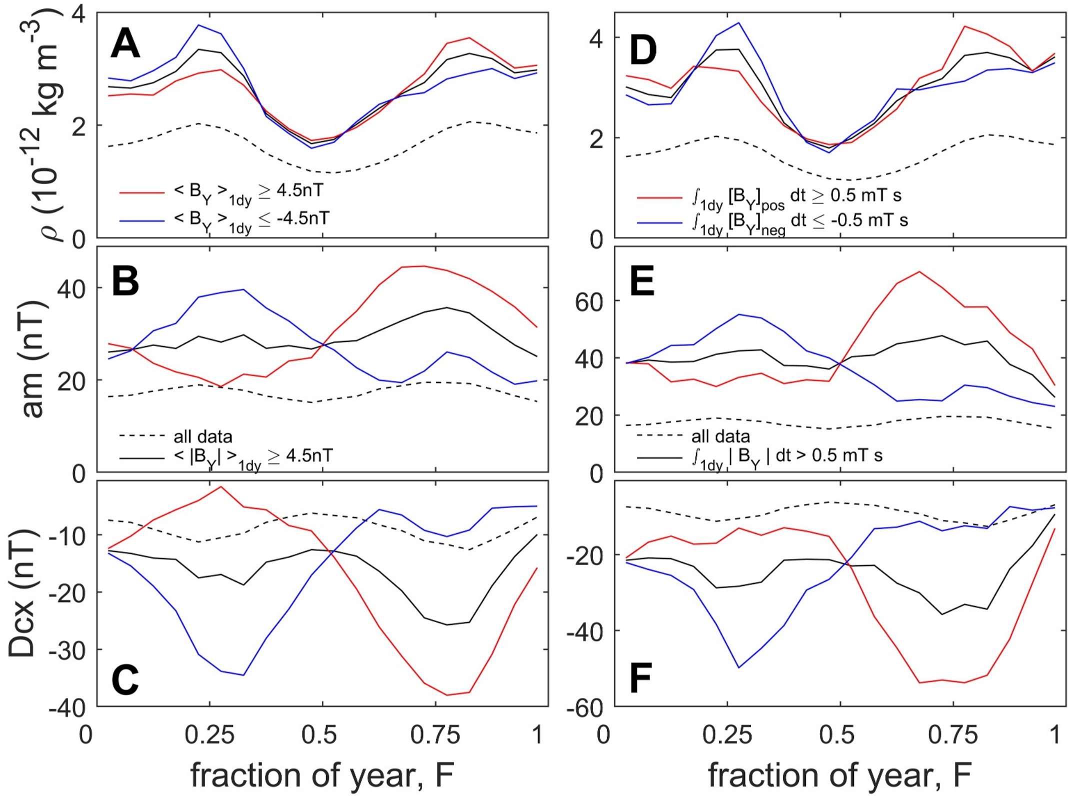

Figure 6. Variation of average values with the fraction of the calendar year, F. Mean values are taken in 20 bins of F. The top row (parts a and d) are for the thermospheric densities ρ. (b) and (e) are for the *am* geomagnetic index. (c) and (f) are for the *Dcx* geomagnetic index. The left-hand panels (a–c) are sorted by the mean values $\langle [B_Y]_{GSEQ} \rangle_{1dy}$ with days with greater than +4.5 nT in red and days with less than −4.5 nT in blue. The right-hand panels (d–f) are sorted by the integrated values $\int_{1dy} B_p dt > 0.5 \times 10^{-3}\ T\ s$ with days with greater than $+0.5 \times 10^{-3}\ T\ s$ in red and days with less than $-0.5 \times 10^{-3}\ T\ s$ in blue. The black lines are if both categories are averaged and the dashed lines are the means for all data.

3.2. Removing the Annual Variation in Thermospheric Densities, ρ

To accurately measure the equinox peaks we need to separate the semiannual variation from the annual variation which is clearly present as values of ρ around the December solstice ($F \approx 1$) are higher than those around the June solstice ($F \approx 0.5$). This annual variation in ρ follows the 3.3% variation in the Sun-Earth distance, r, which minimizes in early January and peaks in early July. This causes a $1/r^2$ variation (of amplitude 10.9%) in the EUV irradiance incident on the Earth.

The best-fit annual variation, fitted to the solstice values, is subtracted out from the variations for the two polarities of $[B_Y]_{GSEQ}$ in Figure 7. Note that the peaks are shifted slightly toward the summer solstice by subtracting the annual variation. Figure 7 marks the equinoxes (at $F = 0.220$ and $F = 0.730$) with vertical black dashed lines but also the times of the peak R-M effect that occur slightly later than their respective equinox (at $F = 0.258$ and $F = 0.780$), as demonstrated by Figure 5 of Lockwood, Owens, Barnard, Haines, et al. (2020): these times are marked by the vertical green dashed lines. For these times we mark the peak of the semiannual variations with dots. The black dots give the peaks for the equinox favored by the R-M effect and the orange dots are the unfavored peaks we label these values ρ_F and ρ_U, respectively. Hence the separations of the black and orange dots $(\rho_F - \rho_U)$ are estimates of the amplitude of the semiannual variation caused by the R-M effect and the ρ_U values give the amplitude of the sum of all other mechanisms contributing to the equinox peaks at this time. However, we have to place a caveat on this because we are using daily data and within the day there will be intervals of "minority" polarity of IMF $[B_Y]_{GSEQ}$ which will enhance the unfavored peak value ρ_U by the R-M effect, so the R-M effect will have contributed a bit to the values given by the orange dots. The potential magnitude of this contribution will be discussed later.

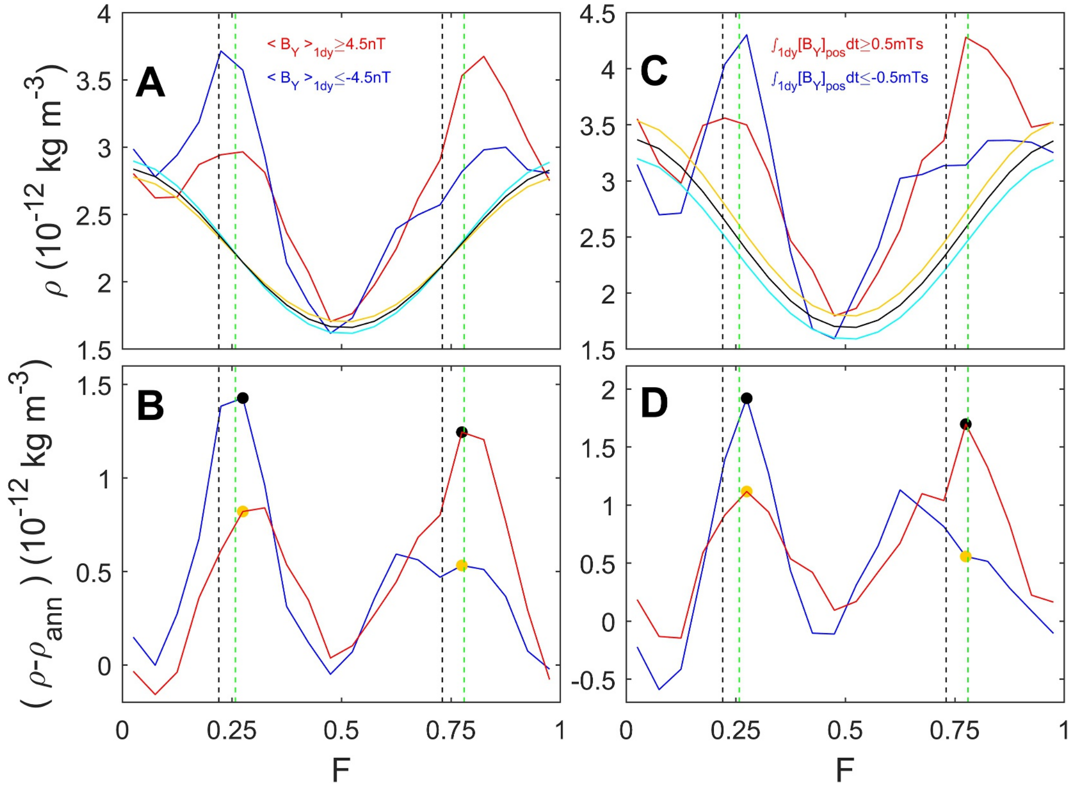

Figure 7. Allowance for the annual variation. The red and blue curves in (a) and (c) are those shown in parts (a) and (d) of Figure 6 and use the means $\langle [B_Y]_{GSEQ} \rangle_{1dy}$ and the integrals $\int_{1dy} B_p dt$, respectively, to determine the dominant polarity of $[B_Y]_{GSEQ}$. The annual variation of $1/r^2$, where r is the Sun-Earth distance, is fitted to the solstice values giving the cyan and orange annual variations for $[B_Y]_{GSEQ} < 0$ and $[B_Y]_{GSEQ} > 0$. These are averaged to give the background annual variation shown in black, which in in Parts (b) and (d) are subtracted out from the variations with F shown in (a) and (c). The dashed black lines are the times of the equinoxes and the dashed green lines are the times of the peak R-M effect. The black and orange dots mark the peaks for the favored and unfavored equinox for the polarity of $[B_Y]_{GSEQ}$ considered.

3.3. The Contribution of the R-M Effect to the Semiannual Variation in Thermospheric Density, ρ

Table 1 investigates the relative magnitudes of the semiannual variations attributable to the R-M and to other contributions using the values shown by dots in the lower panels of Figure 7. In this Table, ρ_{FM} and ρ_{UM} are the favored and unfavored peaks for the March equinox and ρ_{FS} and ρ_{US} are the favored and unfavored peaks for the September equinox. We make four estimates of the R-M and the "other" contributions: for the two equinoxes separately and for each for the two methods of determining the majority polarity of $[B_Y]_{GSEQ}$. Table 1 shows that these four estimates reveal that the R-M effect accounts for between 42.5% and 68.0% of the total semiannual variation with a mean value of 54.7%. The sort using integrated B_p values yields an R-M effect amplitude that is between 8% and 10% larger than that found by sorting by the means of $[B_Y]_{GSEQ}$: we can attribute much of this to the effect of the minority $[B_Y]_{GSEQ}$ polarity population in the daily averaging intervals.

3.4. The Effect of Minority Y-Component Intervals in Daily Thermospheric Density Means

In making the variations with F shown in the left-hand panels of Figure 6, we made two assumptions. The first is that it was appropriate to use daily data. This choice is because we have daily values of the thermospheric densities, ρ. The second choice was to select the polarities of the Y component of the IMF (in GSEQ) above a threshold. For the mean values, $\langle [B_Y]_{GSEQ} \rangle_{1dy}$, a threshold $T = 4.5$ nT was adopted (i.e., the data were sorted into $<[B_Y]_{\mathrm{GSEQ}}>_{1dy} > T$ and $<[B_Y]_{\mathrm{GSEQ}}>_{1dy} < -T$). Both the amplitude of the total semiannual variation and the difference between the F variations for two polarities increase with the value of T adopted. To illustrate the method we adopt an initial value of $T = 4.5$ nT: this is sufficiently large to make the difference between the

Table 1
Quantification of the R-M Effect Contribution to the Semiannual Variation in Thermospheric Densities: ρ_{FM} and ρ_{UM} Are the Favored and Unfavored Peaks (for the IMF $[B_Y]_{GSEQ}$ Polarity Given in the Second Column) for the March Equinox Whereas ρ_{FS} and ρ_{US} Are the Favored and Unfavored Peaks for the September Equinox

Interval: Name	$[B_Y]_{GSEQ}$ polarity	Symbol	Value using $\langle[B_Y]_{GSEQ}\rangle$	Value using $\int[B_p]_{GSEQ}dt$	Units
March Equinox	<0	ρ_{FM}	1.428	1.920	10^{12} kg m^{-3}
March Equinox	>0	ρ_{UM}	0.821	1.117	10^{12} kg m^{-3}
September Equinox	>0	ρ_{FS}	1.245	1.697	10^{12} kg m^{-3}
September Equinox	<0	ρ_{US}	0.532	0.557	10^{12} kg m^{-3}
March:R-M range	–	$R_M = \rho_{MF} - \rho_{MU}$	0.607	0.803	10^{12} kg m^{-3}
March:other range	–	$O_M = \rho_{MU}$	0.821	1.117	10^{12} kg m^{-3}
September:R-M range	–	$R_S = \rho_{FS} - \rho_{US}$	0.713	1.140	10^{12} kg m^{-3}
September:other range	–	$O_S = \rho_{US}$	0.532	0.557	10^{12} kg m^{-3}
March % R-M effect	–	$100R_M/(R_M + O_M)$	42.5	50.5	%
Sept. % R-M effect	–	$100R_S/(R_S + O_S)$	57.3	68.0	%

equinox peaks readily detectable but is not so large that it significantly increases the noise because sample numbers are too low. However, we need to consider what effect this will have had on the magnitude of variations with F, and this is done in Section 3.6.

In addition, there will be effects associated with the averaging timescale of the data used. The reason is that neither of the two ways that we use to define the dominant polarity of $[B_Y]_{GSEQ}$ takes into account the fact that the minority polarity intervals in a day will contribute, via the R-M effect, to the unfavored equinox peak and so make a contribution to the apparent "other" semiannual variation. High time resolution data pose a problem: we do have 1-min geomagnetic indices, such as the SuperMAG indices, but these are compiled from northern hemisphere stations only and so cannot be used in this context. One data set we do have at high resolution are the Omni interplanetary data which can be used to make a high resolution predictor of the terrestrial response. These interplanetary "coupling functions" have been reviewed by Lockwood and McWilliams (2021) but there are many pitfalls in their derivation and use, as discussed by Lockwood (2022). In general, they work best when compiled from the highest resolution data of the component parameters and then averaged (as opposed to averaging the components and then combining them) (Lockwood, 2022; Lockwood et al., 2019a). To look at these effects, we study the known effect on variations in a parameter that is central to the R-M effect and which, unlike for ρ, we can compute for all averaging timescales and thresholds. For this purpose, we use the estimated power input to the magnetosphere P_α given by Equation 3.

Figure 8 gives us an estimate of the effects of the minority polarity intervals during a day, and of the threshold T adopted. It shows the variations with F of the estimated of the normalized power input to the magnetosphere $P_\alpha/\langle P_\alpha\rangle$. Part a shows the results for the two polarities of $[B_Y]_{GSEQ}$ for the 1-min data and a threshold value T of zero. Part b shows the results for the 1-day averages of data and a threshold value T of zero and Part c shows the results for the 1-day averages of data and a threshold value $T = 4.5$ nT, as used in the left-hand column of Figure 6.

Visually these three sets of normalized F variations look quite similar. To enable a better comparison in Part d we plot the differences Δ between the positive and negative $[B_Y]_{GSEQ}$ variations: Δ_A (in mauve) is for the variations shown in part a, Δ_B (in orange) is for the variations shown in part b and Δ_C (in black) is for the variations shown in part c. Comparing Δ_A and Δ_B we find that Δ_A is the larger by 1.65, whereas Δ_C is larger than Δ_B by 1.38. The net effect of both the averaging timescale and the threshold makes Δ_A larger than Δ_C by 1.20. Given that Δ_C is the amplitude of the P_α variation for the threshold and averaging timescale used in column 4 of Table 1 to estimate the amplitude of the R-M effect, this implies that this column of Table 1 underestimates the amplitude of the R-M effect by this factor of 1.20 because of the hidden effect of the minority polarity $[B_Y]_{GSEQ}$ in the 1-day averages.

It is not certain that these figures for P_α would also apply directly to our estimation of the R-M effect on the semiannual variation in the thermospheric densities ρ but, they do give an indication of the likely hidden effect of the minority polarity field in the daily averages. Applying the amplification by a factor 1.20 to the values in the 4^{th} column of Table 1 (derived using the means of $[B_Y]_{GSEQ}$) results in a corrected estimates of the R-M mechanism

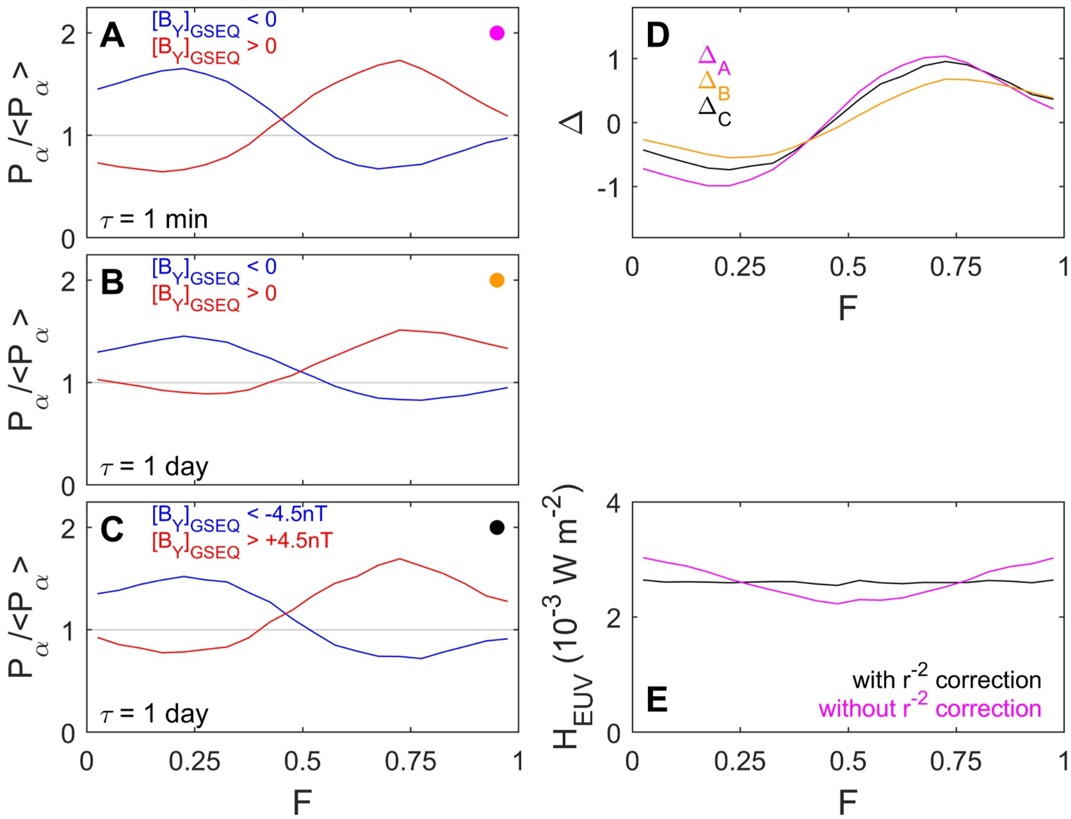

Figure 8. Analysis of the effects of averaging and threshold (T) used in deriving the variations with F. Parts (a–c) show the variations of the normalized estimate of the power input into the magnetosphere $P_\alpha/\langle P_\alpha\rangle$ (see Equation 3) for positive $[B_Y]_{GSEQ} > T$ (in red) and negative $[B_Y]_{GSEQ} < -T$ (in blue). We normalize P_α in this way as it removes the dependence of some parameters, such as Earth's magnetic moment M_E that contribute to the constant K in Equation 3. Part (a) is for 1-min averages and $T = 0$. Part (b) is for 1-day averages and $T = 0$. Part (c) is for 1-day averages and $T = 4.5$ nT and so mirrors the sort carried out on the thermospheric densities shown in part (a) in Figure 6. Part (d) of shows the differences Δ, between the means for positive and negative and $<[B_Y]_{GSEQ}>$: Δ_A (in mauve), Δ_B (in orange), and Δ_C (in black) are for the variations shown in Parts (a–c), respectively. For $T = 0$, the amplitude of the near-sinusoidal variations in Δ is larger for 1-min data than for the 1-day data. For the 1-day data the variation for $T = 4.5$ nT is larger than that for $T = 0$. The net result is that the employed analysis (1-day averages with $T = 4.5$ nT, black line) gives a similar but slightly smaller amplitude of variation than 1-min data with $T = 0$ (mauve line). (e) shows the variation of the EUV heating index, as deduced from fluxes leaving the Sun from measurements by the EVE instrument of SGO, after an $1/r^2$ correction for the annual variation in the distance r between the Sun and the Earth has been implemented (in black). The mauve line is for the fluxes incident in the Earth (i.e., without the $1/r^2$ correction).

contribution of 51.0% for the March equinox and 68.4% for the September equinox. With this correction these values become very similar to those obtained using the integrated B_p values (given in the 5th column of Table 1), which are 50.5% for March and 68.0% for September. There may be some underestimation in the estimate in column 5 of Table 1 because of the minority polarity effect but any correction factor would be considerably smaller than 1.20. Averaging the two methods gives 50.5% for March and 68.2% for September, and averaging the two yields 60% which is our best estimate of the average contribution of the R-M effect to the total semiannual variation in the 1996–2025 interval studied for this threshold of IMF of $|<[B_Y]_{GSEQ}>| = 4.5$ nT.

3.5. The Annual Variation in EUV Heating Effects

Part e of Figure 8 checks that, as expected, the last possible cause of the semiannual variation in ρ, namely a semiannual variation in the EUV heating, is not a factor. In principle, it would be possible that the annual variation of Earth's heliographic latitude could give a semiannual variation via the "axial" effect if there was a persistent variation of EUV irradiance with that latitude. To quantify the thermospheric heating effect of solar EUV radiation, we use observed spectra from the Extreme Ultraviolet Variability Experiment (EVE) instrument on

NASA's Solar Dynamics Observatory (SDO) satellite which is in an inclined geosynchronous orbit around the Earth (Woods et al., 2012), and which covers the wavelength range from 1 nm to 120 nm. The spectral intensities are multiplied by model heating efficiencies of the kind developed by Torr et al. (1980). We use the values for low in the thermosphere (altitude, $h = 120$ km) derived by Solomon and Qian (2005), which are also deployed in the TIE-GCM thermosphere-ionosphere coupled model (Qian et al., 2013). These are linearly interpolated to the EVE wavelengths. The resulting heating, integrated over the EVE wavelength band is here called the "EUV heating index," H_{EUV}. For the black line in Part d of Figure 8 the spectral irradiances have been corrected for the variation of the Sun-Earth distance r and so this line gives the EUV flux emitted from the Sun. It can be seen there is no hint of any variation with F. For the mauve line, the $1/r^2$ correction has been removed and we see the weighted integral of the spectral irradiances that reach Earth. The annual variation in the EUV heating that is a dominant factor in driving the annual variation in ρ can be seen, but there is no hint of a semiannual variation.

3.6. A Sensitivity Study of the Effect of the Sort Thresholds Adopted

In this section we look at the effect of the IMF $\langle [B_Y]_{GSEQ} \rangle_{1dy}$ sort threshold, T. This is done by varying T between 0 and 6 nT in steps of 0.01 nT. This causes the number of daily means to fall from 10,674 (an average of 553.7 per F bin) to 364 (an average of 18.2 per F bin). For sample sizes lower than this, considerable noise is introduced into the variations with F and the semiannual peaks cannot be accurately defined.

Figure 9 illustrates the variations with F of thermospheric and geomagnetic data for four selected values of T (0, 3 nT, 5 nT and 6 nT shown in columns 1, 2, 3 and 4, respectively). For $T = 0$ we are using all the days in the data set except those for $<[B_Y]_{GSEQ}> = 0$. It can be seen in parts Aa and Ba that the R-M effect cannot be detected as both peaks for $[B_Y]_{GSEQ} > 0$ (in red) are bigger than those for $[B_Y]_{GSEQ} < 0$ (in blue). This is almost certainly because of a dominance of the March peak in other mechanisms that is discussed in the next section. However for the other values of T we can resolve a clear R-M effect in ρ and $\rho - \rho_{ann}$. This R-M effect grows in amplitude, as it does for the geomagnetic indices am (third row) and Dcx (bottom row).

Using the method described by Table 1, we define the amplitudes of the R-M contribution and the "other" contribution to the semiannual variation in ρ ($\delta\rho_{RM}$ and $\delta\rho_O$) for each value of T (0:0.01:6])—without any allowance for the effects of the threshold or averaging: the results are shown by the blue and green lines, respectively, in Figure 10a. It can be see that the two are approximately equal for $T = 4.5$ nT (as found in the previous section) but the R-M effect dominates for larger T and the other mechanism for lower T. Part b shows the corresponding variations with T of the semiannual variations in Dcx (mauve line) and am (in black), respectively δDcx_{sa} and δam_{sa}. Part d plots δDcx_{sa} and δam_{sa} against the $\delta\rho_{RM}$ value for the same T. The noise introduced by lower sample numbers becomes apparent at the larger T but a near-linear relationship (shown by the fitted liner regression line) is apparent in both cases.

The mauve line in parts c and f show the variations with T of the mean values of am and Dcx, respectively. These lines are superposed on colored pixels showing the normalized distributions of the geomagnetic index as a function of T. Although the mean values of the two indices behave in the same way (rising to greater activity levels as T is increased), the distributions reveal a difference: for am the mode value increases with the mean and the distribution shift to higher activity levels (and broadens) with increased T; for Dcx, however, the mode stays constant near zero and the relative importance of events of large negative Dcx events grows as T is increased.

A feature of note in part a is that the "other" (non R-M) contribution grows with T. This is expected for the R-M effect (the blue line) but not the other contributions. This may, in part, be because the other contribution still contains some R-M effect, as we would expect to be the case because of the effect of the minority polarity intervals in the daily averages, as discussed earlier. However, there is another influence at work here. Part e shows the variations of the EUV heating index, H_{EUV}, with T. There is a small rise with T that will have caused some or all of the rise in the amplitude of the other mechanisms contributing to the semiannual variation. This arises because there is some correlation between H_{EUV} and $|[B_Y]_{GSEQ}|$ in that both vary over the solar cycle. However the rise in average H_{EUV} with T is small compared with the amplitude of the solar cycle variation in 27-day averages of H_{EUV} (as is demonstrated by part e of Figure 10).

The part of the "other" contribution that could be contributed by the R-M effect because of the minority polarity intervals remains hard to quantify. Figure 11 provides an interesting, independent, perspective on this. It is based on the quietest 10% of geomagnetic data (given by the ranges $am < 6$ nT in the left-hand plots and

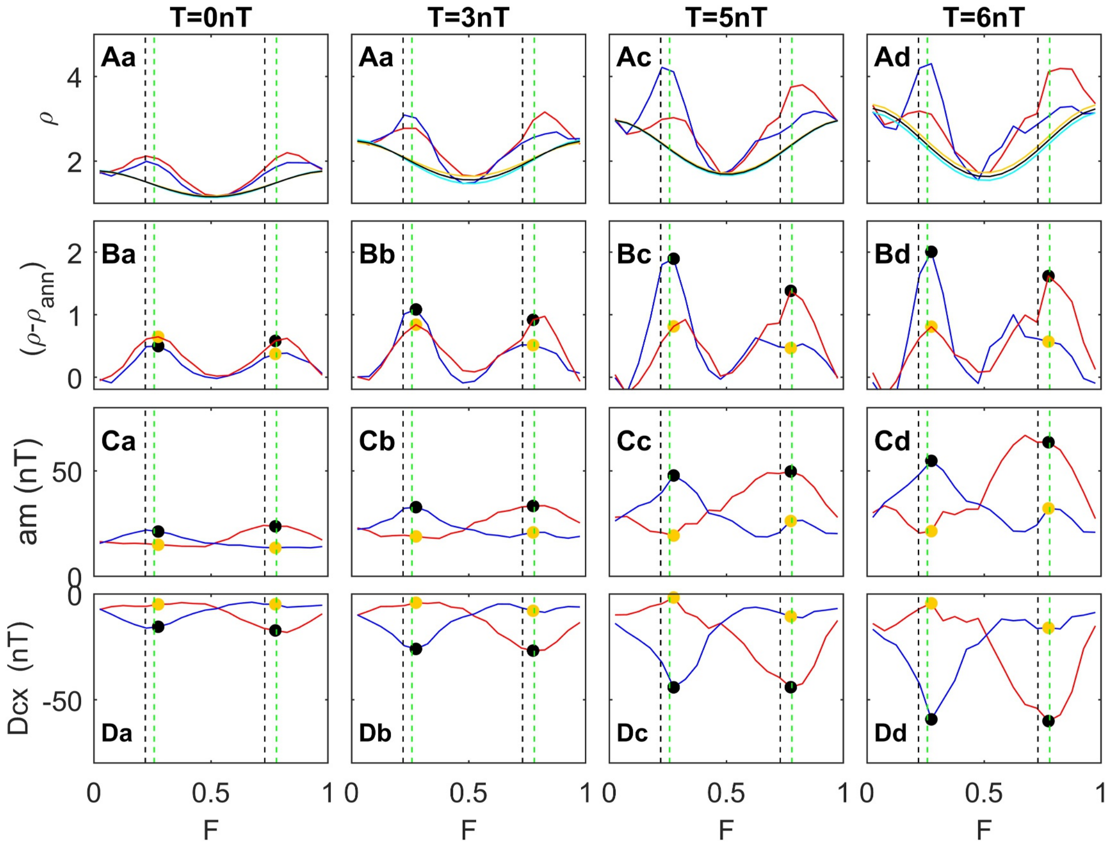

Figure 9. Variations with F using mean values and four values of the threshold T. Panels in the top row (labeled with an upper case A) show the variations in ρ in the same format as Part a of Figure 7. The panels of the second row (the B panels) are the same format as Part b of Figure 7 and show semiannual variations with the annual variation subtracted $\left(\rho - \rho_{ann}\right)$. The third row (the C panels) show the variations in the *am* geomagnetic index (red/blue for positive/negative IMF $[B_Y]_{GSEQ}$, respectively) and the bottom row (the D panels) show the corresponding variations in Dcx. The left-hand column (the panels labeled with a lower case a) are for a threshold T of zero (i.e., all data except those with $<[B_Y]_{GSEQ}> = 0$). The second, third and fourth columns (panels labeled b–d are for $T = 3$ nT, $T = 5$ nT and $T = 6$ nT.

$-2 < Dcx < 1$ nT in the right-hand plots). The 10% selection gives 53 samples in each F bin which is enough to keep the noise low but a lower value introduced considerable noise into the F variations.

The upper panels in Figure 11 give the mean values of the thermospheric density ρ the in lower panels the best-fit annual variation has been subtracted $\left(\rho - \rho_{ann}\right)$. There is no IMF $[B_Y]_{GSEQ}$ sort used in this case. The orange values mark the equinox peaks which, if we neglect any residual contribution as negligible because of the low geomagnetic activity levels, gives the amplitude of the "other" contribution. We note that the March peak is considerable larger than the September one, a feature discussed in the next section. The average of the four peaks is 0.372 nT. The green line in part a of figure has a minimum at the lowest T of 0.472 nT and so it appears that the other mechanism has been overestimated by 20.5%. This is very close to the factor of overestimation found for $T = 4.5$ nT using the P_α metric at one-minute resolution.

In Figure 10a we apply this 20% correction for the minority polarity $[B_Y]_{GSEQ}$ to all values of the amplitude of the "other" seminaual variation, $\delta\rho_O$ (in green) at all T to give the corrected variation $\delta\rho_{Oc}$ (in orange) and then correspondingly correct the RM amplitude $\delta\rho_{RMc}$ (in blue) by adding $\left(\delta\rho_O - \delta\rho_{Oc}\right)$ to give $\delta\rho_{RMc}$ (in cyan). It can be seen with this correction the R-M contribution dominates for $T > 4$ nT.

3.7. Asymmetry of the Equinox Peaks

It is noticeable that of the two peaks of the semiannual variation in ρ, the March equinox is generally the greater (see Figure 9). This has been noted in a number of papers (Lomidze et al., 2023; Xiong et al., 2018; J. Yue

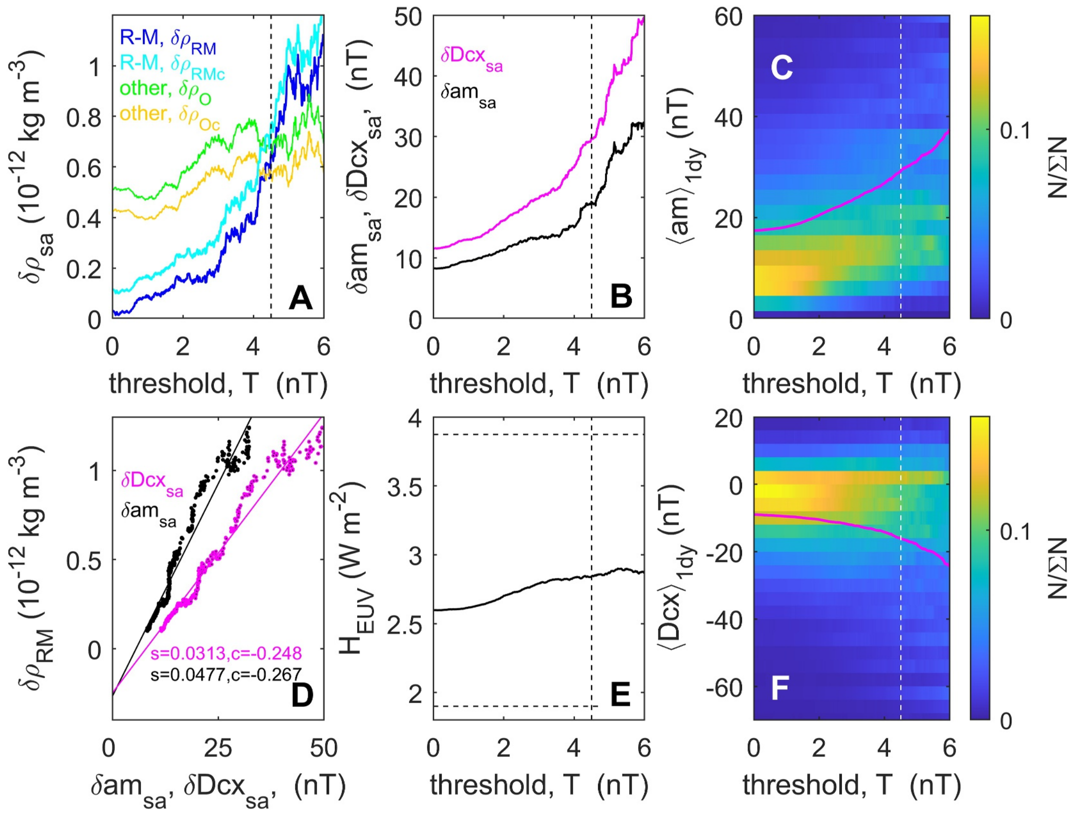

Figure 10. Analysis of various effects of varying the threshold T from 0 to 6nT in steps of 0.01. (a) the contributions of the R-M ($\delta\rho_{RM}$, in blue) and other ($\delta\rho_O$, in green) mechanisms to the semiannual variation in density, as determined in the left hand column of Figure 7 and in Figure 9. The cyan and orange lines are corrected for the 20% effect in $\delta\rho_O$ caused by the minority polarity intervals in a day (respectively, $\delta\rho_{RMc}$ and $\delta\rho_{Oc}$). (b) The amplitude of the semiannual variation in the *am* and *Dcx* geomagnetic indices, δam_{sa} and δDcx_{sa} (black and mauve lines, respectively). (c) The variation of daily means of *am* (mauve line). The colors show the variation of the distribution of $\langle am \rangle_{1dy}$ with the pixels (4 nT wide) color-coded by the number of samples N divided by the total number of samples for the T in question, ΣN. (d) the corrected amplitude of the semiannual R-M variation $\delta\rho_{RMc}$ (shown in cyan in part a) as a function of the semiannual variation amplitudes in *am* (black dots) and *Dcx* (mauve dots) shown in (b). (e) The EUV heating index, H_{EUV}. The horizontal dashed lines give the minimum and maximum of the 27-day means $\langle H_{EUV} \rangle_{27dy}$ which define recent solar cycle amplitudes. (f) The same as Part (c) for the *Dcx* index.

et al., 2019) and a variety of causal mechanisms proposed. This is, if anything, inconsistent with the geomagnetic activity peaks in Figures 6 and 9 that tend to be of equal magnitude or slightly greater for the September equinox.

Figure 1 of Lockwood, Owens, Barnard, Haines, et al. (2020) shows the annual variations of the aa_H geomagnetic index since 1868: in some years the September equinox dominates whereas in others the March peak dominates. Hence the dominance of one equinox over the other due to the R-M effect seems to be almost random and will depend on asymmetries of the $[B_Y]_{GSEQ}$ distribution around zero.

Figure 12a shows the distribution of all $[B_Y]_{GSEQ}$ values for the interval studied here (1996–2025). The mauve line is the same distribution, but with the X axis flipped in direction to reveal asymmetries. The peak for positive $[B_Y]_{GSEQ}$ is slightly narrower than for negative $[B_Y]_{GSEQ}$ which means there are slightly more larger positive values than there are negative values of the same magnitude. However the asymmetry is very slight. If we sort the data by the two equinoxes, a slightly different picture emerges. Figure 12b plots the data for 0.25-year intervals centered on the March peak of the R-M effect (in red) and on the September peak (in blue). Both distributions show a slight dominance of the $[B_Y]_{GSEQ} < 0$ peak: this asymmetry will enhance the March peak of the R-M effect whilst reducing the September peak, both effects adding to the dominance of the March peak. When we look at the R-M contributions to the equinox peaks (the difference between the black and orange dots in the second row of parts Ba to Bd of Figure 9), we see the March peak of the R-M contribution is indeed the larger for the large values of T but for $T = 3$ the September peak is slightly the larger. Hence the R-M effect may be

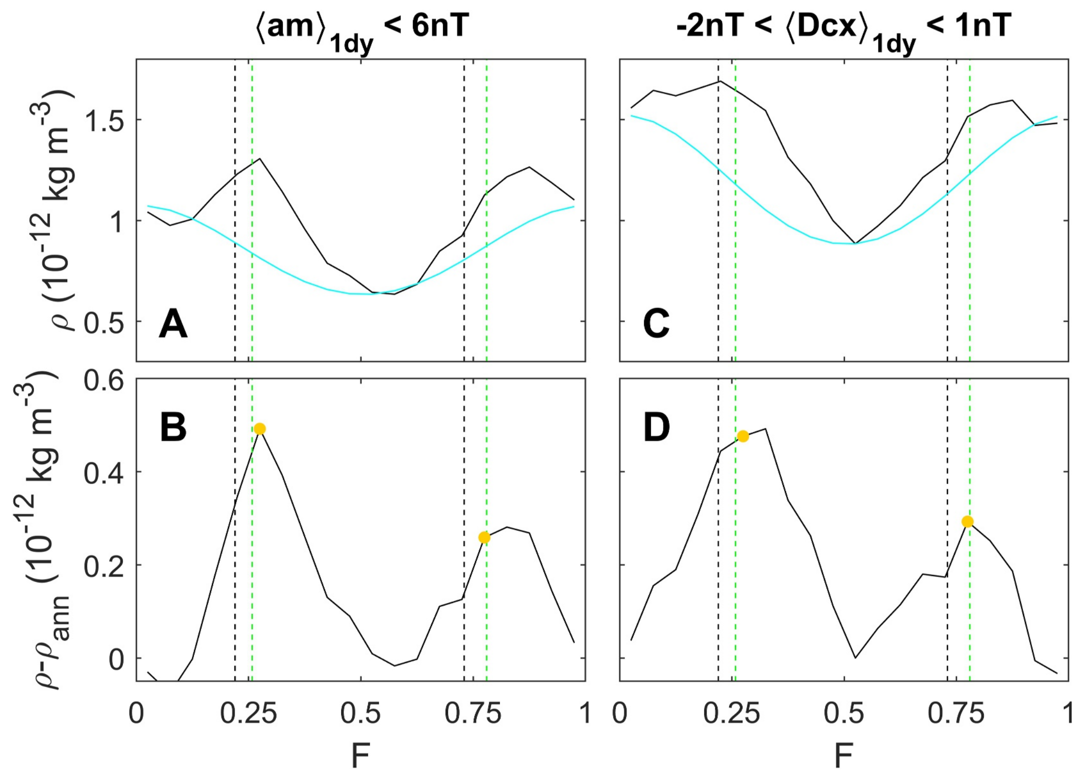

Figure 11. Semiannual variations in ρ for very the quietest 10% of geomagnetic conditions in the same format as Figure 9. The left hand column is for *am* below 6 nT and the right column for *Dcx* between -2 nT and $+1$ nT. In the upper panels the cyan line is the best-fit annual variation which is subtracted in the lower panels.

contributing to the March peak but only for larger values of $|<[B_Y]_{GSEQ}>|$ revealed by high T. This fits with the finding by Xiong et al. (2018) who found that the March peak in global thermospheric density, ρ was the greater at high activity levels but the September peak was greater in quiet times. Therefore, it is possible that the asymmetry of the IMF $[B_Y]_{GSEQ}$ distribution at the equinoxes found here is (at least partially) responsible for the dominance of the March peak in ρ, via the R-M effect. This is not necessarily inconsistent with a dominance in the September peak in the geomagnetic indices because Figures 9 and 10 show that the R-M effect on the geomagnetic indices can be seen for very low values of T (dominated by low $|<[B_Y]_{GSEQ}>|$) at which no R-M effect can be detected in ρ: hence the net effect of averaging over a wide range of $|<[B_Y]_{GSEQ}>|$ can be different in the geomagnetic and thermospheric density data.

4. Discussion and Conclusions

We have studied the influence that the Russell-McPherron (R-M) mechanism, which controls the average pattern of solar-wind magnetosphere coupling, has on the semiannual variation in thermospheric densities. We identify the influence of the R-M effect using the fact that it, uniquely, introduces a dependence on the polarity of the Y-component of the IMF in the GSEQ frame.

Cliver et al. (2000) rightly described studies of the implications of time-of-year/time-of-day (F-UT) patterns as a matter of both "valleys" and "mountains": in other words, there are both maxima and minima to consider. Studies of coupling functions and of the semiannual variation in geomagnetic activity show that half-wave rectification (Equation 1) is not the best model for predicting power input to the magnetosphere, as it yields the mountains but not the valleys. For better-performing coupling functions (such as given in Equations 2 and 3) there is partial cancellation of the peaks in the R-M F-UT pattern for one polarity of IMF $[B_Y]_{GSEQ}$ by the minima at the same F and UT for the opposite $[B_Y]_{GSEQ}$ polarity (Lockwood, McWilliams, et al., 2020; Lockwood, Owens, Barnard, Haines, et al., 2020). Hence, the importance of a realistic coupling function is that for the unfavored IMF $[B_Y]_{GSEQ}$ at a given equinox the energy input into the magnetosphere is not just a flat base-level value but shows a minimum (a "valley"). These minima can be seen in the second row of Figure 3 of the present paper when compared with the idealized R-M predictions based on half wave rectification, shown in the top row. This partial cancellation of the "mountains" and "valleys" of the F - UT pattern means that without separating the IMF $[B_Y]_{GSEQ}$ polarities, as has been the case in many studies, the R-M effect will be seriously underestimated. In addition, we note that Ap, ap or kp are often used to quantify geomagnetic effects and these strongly imprint the way they are constructed onto the F - UT pattern (Lockwood, Chambodut, et al., 2019) which, in turn, strongly influences the detection of the R-M effect.

In the present paper we have reduced this partial cancellation of the two polarities of IMF by separating the two. However, there is still a problem because we have only daily data on the global mean thermospheric density, ρ, and full days with only one polarity of the IMF Y-component are rare. This gives the "minority polarity" problem whereby the contributions to the equinox peak caused by the majority IMF Y-component polarity in a day are partially canceled by the troughs caused by the minority polarity. Hence in this paper we have needed to develop corrections to allow for this effect.

Figure 10a shows that if we only use the IMF $[B_Y]_{GSEQ}$ polarity test with no correction for the minority polarity in a day, the R-M mechanism for all data ($T = 0$) contributes just 0.025×10^{-12} kg m^{-3} to the equinox peaks in ρ which is only 5% of the total. In addition to the minority $[B_Y]_{GSEQ}$ polarity effect, there is a second problem that masks the R-M effect at low IMF $|<[B_Y]_{GSEQ}>|$: this arises because the asymmetric March peak generated by the other (non R-M) mechanisms contributing to the semiannual variation in ρ causes us to fail to identify the R-M mechanism and so contributes to the low estimate of the R-M mechanism contribution at $T = 0$.

By using the amplitude of the semi-annual variation seen when geomagnetic activity is very low (and hence the R-M effect is very weak), Figure 11 reveals that our test overestimates the non R-M contributions by at least 20% and applying this correction raises the amplitude of the R-M contribution to 0.101×10^{-12} kg m^{-3} which is 21% of the total. This is likely to still be an underestimate as there will be some, albeit small, R-M effect even in Figure 11 because the geomagnetic activity is weak but not absent. Looking at the effects of averaging timescale and the adopted threshold T on high resolution (1-min) estimates of power input to the magnetosphere also yields a 20% correction factor estimate for the R-M effect contribution in daily data.

We find that the contribution of the R-M mechanism rises with the IMF Y-component threshold, T, as one would expect and, without the 20% correction, the R-M effect becomes the dominant contribution to the semiannual variation in thermospheric densities at $T = 4.5$ nT. If we implement the 20% correction discussed above, this happens at $T = 4$ nT which, from Figure 12, occurs 15% of the time. The largest T for which the numbers of available samples allows us to detect reliable variations with F is $T = 6$ nT and at this threshold the R-M mechanism contributes 63% of the semi-annual variation. There is one other notable statistic of this rise of the R-M contribution with T: from Figure 12 the $T = 2.1$ nT threshold applies 50% of the time and Figure 10a shows that, with the correction for minority polarity, yields a 27% R-M contribution.

The results clearly demonstrate that during intervals of large IMF $|<[B_Y]_{GSEQ}>|$ (above 4 nT), the R-M effect is responsible for over half of the semiannual variation in the mean thermospheric densities at altitudes between 450 and 530 km. We have repeated the study using NRL data for different altitudes (not shown) and find the percentage contribution of the R-M effect is almost constant over the altitude range $300-550$ km and so our result is only very weakly dependent on the altitude of the SWARM satellites. A subsequent paper will present this analysis for the different altitudes down to the minimum of the NRL data set, which is 250 km.

We note that in their model GCM experiment, Qian et al. (2009) needed to supplement the spoon mechanism in order to match the observed amplitude of the semiannual variation. They did so by adding forcing at the base of the thermosphere in the form of waves and tides from the lower atmosphere. Our results suggest that the R-M effect and geomagnetic currents may actually provide some or all of the additional factor that is needed. We also note that, in the interval studied at least, there is a slight asymmetry in the distribution of $[B_Y]_{GSEQ}$ values at the equinoxes favoring negative values. This will cause the R-M effect to slightly enhance the March peak and slightly reduce the September peak. Hence the R-M mechanism may have also contributed to the known dominance of the March peak in ρ.

It is well known that large space weather events cause sudden and large spikes in global thermospheric density, due to the heating effect of induced currents in the ionosphere (Liu & Lühr, 2005; Sutton et al., 2005; Volland &

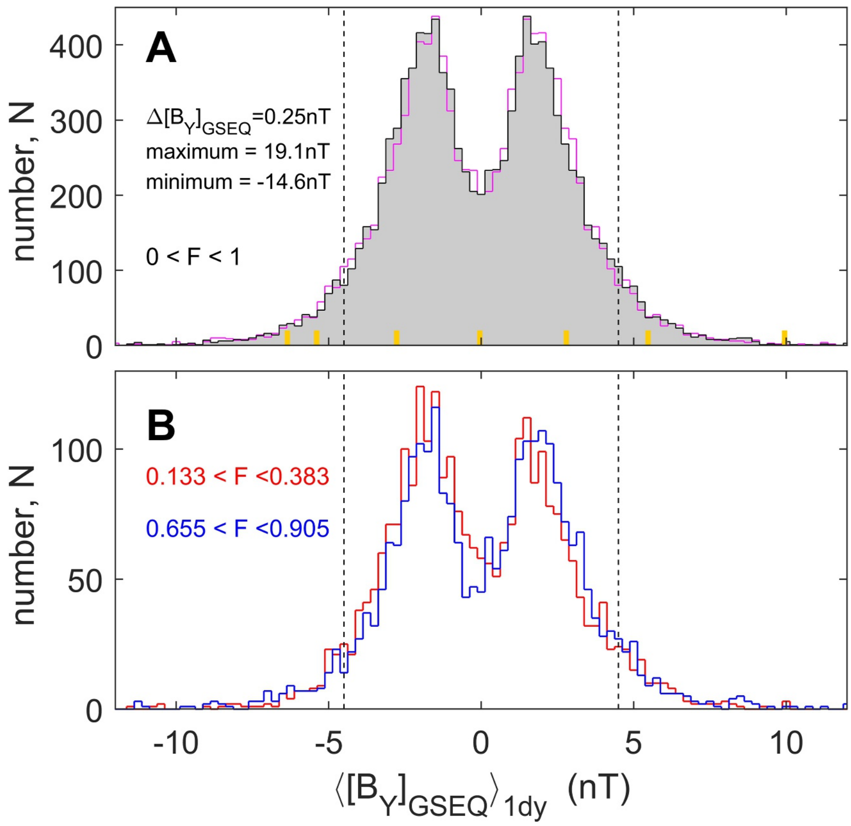

Figure 12. Histograms showing the numbers, N of daily means of IMF $[B_Y]_{GSEQ}$ in 0.25 nT bins. Part (a) is for all the data in the interval studied. The gray filled area is the histogram which has plotted in mauve as mirror image (i.e., the x-axis been multiplied by -1) to reveal any differences between the two polarities of $[B_Y]_{GSEQ}$. Part (b) show the distributions for two quarter-year intervals centered on the predicted peak times of the equinox peaks caused by the R-M effect. Red is for the interval around the March peak and blue for the interval around the September peak.

Mayr, 1971). These enhancements decay away quickly (of order 1–2 dy). The largest geomagnetic storm events are caused by interplanetary transients (particularly ICMEs) with large negative $[B_Z]_{GSEQ}$, the occurrence of which is random in F. However, there is a semiannual variation in moderate geomagnetic events caused by the enhancing/reducing effect (depending on the equinox and the $[B_Y]_{GSEQ}$ polarity) of the R-M mechanism (Lockwood, Owens, Barnard, Haines, et al., 2020). It becomes an interesting question if these moderate events are the source of the R-M driven semiannual variation in thermospheric densities associated detected here or if there is a significant contribution from small geomagnetic disturbances or even quiet-time currents. An analysis of the dependence on geomagnetic activity level of the R-M contribution to the semiannual variation in thermospheric densities will also be presented in a subsequent paper. In addition, the present paper has used data from altitudes between 460 and 520 km. For studies relevant to de-orbitins spacecraft, we need to understand the behavior at all altitudes down to the re-entry altitude (approximately 120 km). We can use the NRL data, but not the SWARM data, for this purpose. However, that restricts the interval of available data to 1967–2019 and the NRL data only extend down to 250 km. The altitude dependence of the R-M effect on thermospheric densities will be the focus of the subsequent publication.

AI Tools Disclosure

AI tools (Connected Papers and Chat GPT) were employed in some aspects this work. They were used to augment the literature search: but any papers revealed that way were then read carefully to check that they did indeed contain the cited information. In addition, AI was used to generate some Matlab modules for the extraction of some of the data from internet sources. These codes were always checked by regenerating various plots of the same data that are already in the literature. AI was not used in any other aspects of the work.

Conflict of Interest

The authors declare no conflicts of interest relevant to this study.

Availability Statement

The data used in this paper are all available on-line and in the public domain. The SWARM thermospheric densities are published by the Technical University Delft, The Netherlands at http://thermosphere.tudelft.nl/. The NRL thermospheric density data set is published by the Naval Research Laboratory, Washington, DC, USA at https://map.nrl.navy.mil/map/pub/nrl/orbit_derived_density/v2.0_1967-2019/orbit-density-ds03-density-values.txt. The interplanetary magnetic field data are available from the Omniweb web pages maintained by NASA's Space Physics Data Facility at Goddard Space Flight Center, Maryland, USA at https://omniweb.gsfc.nasa.gov/. The definitive *Dcx* index (at the time of writing, up to the end of 2016) is available from Oulu University, Finland at http://dcx.oulu.fi/?link=queryDefinite and provisional *Dcx* from http://dcx.oulu.fi/?link=queryProvisional. The geomagnetic *am* index is available from the International Service of Geomagnetic Indices (ISGI) in Strasbourg at https://isgi.unistra.fr/data_download.php. The sunspot number data used were generated by WDC-SILSO/SIDAC, Royal Observatory of Belgium, Brussels and are available from https://www.sidc.be/SILSO/datafiles.

Acknowledgments

The authors are grateful to the many scientists and engineers who contributed to the various data sets that were exploited in this study. We also thank the staff and fund bodies of the several data centers that give access to these data. In particular, we wish to give thanks to: the Technical University Delft, The Netherlands for the SWARM thermospheric densities, The Naval Research Laboratory, Washington, DC, USA for the NRL thermospheric density data set; NASA's Space Physics Data Facility at Goddard Space Flight Center, Maryland, USA for the Omniweb 1-min interplanetary magnetic field data; Oulu University, Finland for the *Dcx* geomagnetic index; the International Service of Geomagnetic Indices (ISGI) in Strasbourg for the geomagnetic *am* index; and WDC-SILSO/SIDAC, Royal Observatory of Belgium, Brussels for the sunspot number data. The authors also thank a variety of funding sources: ML, JoD, CJS and MJO are part-funded by the UK Science and Technology Facilities Council (STFC) Grant UKRI1207 and MJO is also part funded by the UK Natural Environment Research Council (NERC) Grant NE/Y001052/1. CJS is part funded by the NERC Drivers and Impacts of Ionospheric Variability with EISCAT-3D (DRIIVE) project, UKRI Grant NE/W003384/1. LAB is supported by UK Research and Innovation (UKRI) Future Leaders Fellowship MR/Y021207/1.

References

Bartels, J. (1925). Eine universelle tagesperiode der erdmagnetischen aktivität. *Meteorologische Zeitschrift*, *42*, 147–152.

Bowman, B. R., Tobiska, W. K., Marcos, F. A., & Valladares, C. (2008). The JB2006 empirical thermospheric density model. *Journal of Atmospheric and Solar-Terrestrial Physics*, *70*(5), 774–793. https://doi.org/10.1016/j.jastp.2007.10.002

Caan, M. N., McPherron, R. L., & Russell, C. T. (1973). Solar wind and substorm-related changes in the lobes of the geomagnetic tail. *Journal of Geophysical Research*, *78*(34), 8087–8096. https://doi.org/10.1029/JA078i034p08087

Chambodut, A., Marchaudon, A., Menvielle, M., El-Lemdani Mazouz, F., & Lathuillére, C. (2013). The **K** -derived MLT sector geomagnetic indices. *Geophysical Research Letters*, *40*(18), 4808–4812. https://doi.org/10.1002/grl.50947

Cliver, E. W., Kamide, Y., & Ling, A. G. (2000). Mountains versus valleys: Semiannual variation of geomagnetic activity. *Journal of Geophysical Research*, *105*(A2), 2413–2424. https://doi.org/10.1029/1999JA900439

Cortie, A. L. (1912). Sun-spots and terrestrial magnetic phenomena, 1898-1911: The cause of the annual variation in magnetic disturbances. *Monthly Notices of the Royal Astronomical Society*, *73*(1), 52–60. https://doi.org/10.1093/mnras/73.1.52

De La Sayette, P., & Berthelier, A. (1996). The *am* annual-diurnal variations 1959-1988: A 30-year evaluation. *Journal of Geophysical Research*, *101*(A5), 10653–10663. https://doi.org/10.1029/96JA00165

Detman, T. R. (1996). Cross validation comparisons of autonomous ap predictions. In *Proceedings of Workshop on the Evaluation of Space Weather Forecasts* (p. 149). NOAA Environmental Research Laboratories. (Workshop contribution).

Doornbos, E. N. (2012). Thermospheric density and wind determination from satellite dynamics Doctoral dissertation. Retrieved from http://resolver.tudelft.nl/uuid:33002be1-1498-4bec-a440-4c90ec149aea

Emmert, J. T. (2015). Thermospheric mass density: A review. *Advances in Space Research*, *56*(5), 773–824. https://doi.org/10.1016/j.asr.2015.05.038

Emmert, J. T., Dhadly, M. S., & Segerman, A. M. (2021). A globally averaged thermospheric density data set derived from two-line orbital element sets and special perturbations state vectors. *Journal of Geophysical Research: Space Physics*, *126*(8), e2021JA029455. https://doi.org/10.1029/2021JA029455

Emmert, J. T., & Picone, J. M. (2010). Climatology of globally averaged thermospheric mass density. *Journal of Geophysical Research*, *115*(A9), 2010JA015298. https://doi.org/10.1029/2010JA015298

Finch, I. D., & Lockwood, M. (2007). Solar wind-magnetosphere coupling functions on timescales of 1 day to 1 year. *Annales Geophysicae*, *25*(2), 495–506. https://doi.org/10.5194/angeo-25-495-2007

Finch, I. D., Lockwood, M. L., & Rouillard, A. P. (2008). Effects of solar wind magnetosphere coupling recorded at different geomagnetic latitudes: Separation of directly-driven and storage/release systems. *Geophysical Research Letters*, *35*(21), L21105. https://doi.org/10.1029/2008GL035399

Forbes, J. M., Zhang, X., Hagan, M. E., England, S. L., Liu, G., & Gasperini, F. (2017). On the specification of upward-propagating tides for ICON science investigations. *Space Science Reviews*, *212*(1–2), 697–713. https://doi.org/10.1007/s11214-017-0401-5

Fuller-Rowell, T. J. (1998). The "thermospheric spoon": A mechanism for the semiannual density variation. *Journal of Geophysical Research*, *103*(A3), 3951–3956. https://doi.org/10.1029/97JA03335

Guo, D., Lei, J., & Dou, X. (2015). Statistical analysis of thermospheric density response to solar wind sector structure. *Journal of Geophysical Research: Space Physics*, *120*(6), 5076–5086. https://doi.org/10.1002/2015JA021112

Guo, J., Feng, X., Forbes, J. M., Lei, J., Zhang, J., & Tan, C. (2010). On the relationship between thermosphere density and solar wind parameters during intense geomagnetic storms. *Journal of Geophysical Research*, *115*(A12), 2010JA015971. https://doi.org/10.1029/2010JA015971

Huang, Y., Richmond, A. D., Deng, Y., & Roble, R. (2012). Height distribution of Joule heating and its influence on the thermosphere. *Journal of Geophysical Research*, *117*(A8), 2012JA017885. https://doi.org/10.1029/2012JA017885

Jones, M., Emmert, J. T., Drob, D. P., Picone, J. M., & Meier, R. R. (2018). Origins of the thermosphere-ionosphere semiannual oscillation: Reformulating the "thermospheric spoon" mechanism. *Journal of Geophysical Research: Space Physics*, *123*(1), 931–954. https://doi.org/10.1002/2017JA024861

Karinen, A., & Mursula, K. (2005). A new reconstruction of the D_{st} index for 1932-2002. *Annales Geophysicae*, *23*(2), 475–485. https://doi.org/10.5194/angeo-23-475-2005

Karlsson, S. B. P., Opgenoorth, H. J., Eglitis, P., Kauristie, K., Syrjäsuo, M., Pulkkinen, T., et al. (2000). Solar wind control of magnetospheric energy content: Substorm quenching and multiple onsets. *Journal of Geophysical Research*, *105*(A3), 5335–5356. https://doi.org/10.1029/1999JA900297

Kivelson, M. G., & Hughes, W. (1990). On the threshold for triggering substorms. *Planetary and Space Science*, *38*(2), 211–220. https://doi.org/10.1016/0032-0633(90)90085-5

Kokubun, S., McPherron, R. L., & Russell, C. T. (1977). Triggering of substorms by solar wind discontinuities. *Journal of Geophysical Research*, *82*(1), 74–86. https://doi.org/10.1029/JA082i001p00074

Lamy, P. L., Floyd, O., Boclet, B., Wojak, J., Gilardy, H., & Barlyaeva, T. (2019). Coronal Mass Ejections over solar cycles 23 and 24. *Space Science Reviews*, *215*(5), 39. https://doi.org/10.1007/s11214-019-0605-y

Lei, J., Matsuo, T., Dou, X., Sutton, E., & Luan, X. (2012). Annual and semiannual variations of thermospheric density: EOF analysis of CHAMP and GRACE data. *Journal of Geophysical Research*, *117*(A1), 2011JA017324. https://doi.org/10.1029/2011JA017324

Liu, H., & Lühr, H. (2005). Strong disturbance of the upper thermospheric density due to magnetic storms: CHAMP observations. *Journal of Geophysical Research*, *110*(A9), 2004JA010908. https://doi.org/10.1029/2004JA010908

Lockwood, M. (2013). Reconstruction and prediction of variations in the open solar magnetic flux and interplanetary conditions. *Living Reviews in Solar Physics*, *10*. https://doi.org/10.12942/lrsp-2013-4

Lockwood, M. (2019). Does adding solar wind poynting flux improve the optimum solar wind-magnetosphere coupling function? *Journal of Geophysical Research: Space Physics*, *124*(7), 5498–5515. https://doi.org/10.1029/2019JA026639

Lockwood, M. (2022). Solar wind-magnetosphere coupling dunctions: Pitfalls, limitations, and applications. *Space Weather*, *20*(2), e2021SW002989. https://doi.org/10.1029/2021SW002989

Lockwood, M., Bentley, S. N., Owens, M. J., Barnard, L. A., Scott, C. J., Watt, C. E., & Allanson, O. (2019a). The development of a space climatology: 1. Solar wind magnetosphere coupling as a function of timescale and the effect of data gaps. *Space Weather*, *17*(1), 133–156. https://doi.org/10.1029/2018SW001856

Lockwood, M., Bentley, S. N., Owens, M. J., Barnard, L. A., Scott, C. J., Watt, C. E., et al. (2019b). The development of a space climatology: 2. The distribution of power input into the magnetosphere on a 3-hourly timescale. *Space Weather*, *17*(1), 157–179. https://doi.org/10.1029/2018SW002016

Lockwood, M., Chambodut, A., Finch, I. D., Barnard, L. A., Owens, M. J., & Haines, C. (2019). Time-of-day/time-of-year response functions of planetary geomagnetic indices. *Journal of Space Weather and Space Climate*, *9*, A20. https://doi.org/10.1051/swsc/2019017

Lockwood, M., Haines, C., Barnard, L. A., Owens, M. J., Scott, C. J., Chambodut, A., & McWilliams, K. A. (2021). Semi-annual, annual and Universal Time variations in the magnetosphere and in geomagnetic activity: 4. Polar Cap motions and origins of the Universal Time effect. *Journal of Space Weather and Space Climate*, *11*, 15. https://doi.org/10.1051/swsc/2020077

Lockwood, M., & McWilliams, K. A. (2021). On optimum solar wind-magnetosphere coupling functions for transpolar voltage and planetary geomagnetic activity. *Journal of Geophysical Research: Space Physics*, *126*(12), e2021JA029946. https://doi.org/10.1029/2021JA029946

Lockwood, M., McWilliams, K. A., Owens, M. J., Barnard, L. A., Watt, C. E., Scott, C. J., et al. (2020). Semi-annual, annual and Universal Time variations in the magnetosphere and in geomagnetic activity: 2. Response to solar wind power input and relationships with solar wind dynamic pressure and magnetospheric flux transport. *Journal of Space Weather and Space Climate*, *10*, 30. https://doi.org/10.1051/swsc/2020033

Lockwood, M., Owens, M. J., Barnard, L. A., Bentley, S. N., Scott, C. J., & Watt, C. E. (2016). On the origins and timescales of geoeffective IMF. *Space Weather*, *14*(6), 406–432. https://doi.org/10.1002/2016SW001375

Lockwood, M., Owens, M. J., Barnard, L. A., Haines, C., Scott, C. J., McWilliams, K. A., & Coxon, J. C. (2020). Semi-annual, annual and Universal Time variations in the magnetosphere and in geomagnetic activity: 1. Geomagnetic data. *Journal of Space Weather and Space Climate*, *10*, 23. https://doi.org/10.1051/swsc/2020023

Lockwood, M., Owens, M. J., Barnard, L. A., Watt, C. E., Scott, C. J., Coxon, J. C., & McWilliams, K. A. (2020). Semi-annual, annual and Universal Time variations in the magnetosphere and in geomagnetic activity: 3. Modelling. *Journal of Space Weather and Space Climate*, *10*, 61. https://doi.org/10.1051/swsc/2020062

Lomidze, L., Knudsen, D. J., Shepherd, M., Huba, J. D., & Maute, A. (2023). Equinoctial asymmetry in the upper ionosphere: Comparison of satellite observations and models. *Journal of Geophysical Research: Space Physics*, *128*(5), e2022JA031123. https://doi.org/10.1029/2022JA031123

Mayaud, P. N. (1980). *Derivation, meaning, and use of geomagnetic indices* (Vol. 22). American Geophysical Union. https://doi.org/10.1029/GM022

McIntosh, D. (1959). On the annual variation of magnetic disturbance. *Philosophical Transactions of the Royal Society of London. Series A, Mathematical and Physical Sciences*, *251*(1001), 525–552. https://doi.org/10.1098/rsta.1959.0010

Meng, X., Ozturk, D. S., Verkhoglyadova, O. P., Varney, R. H., Reimer, A. S., Semeter, J. L., et al. (2022). Energy deposition by mesoscale high-latitude electric fields into the thermosphere during the 26 October 2019 geomagnetic storm. *Journal of Geophysical Research: Space Physics*, *127*(12), e2022JA030716. https://doi.org/10.1029/2022JA030716

Mursula, K., & Karinen, A. (2005). Explaining and correcting the excessive semiannual variation in the *Dst* index. *Geophysical Research Letters*, *32*(14), 2005GL023132. https://doi.org/10.1029/2005GL023132

Paetzold, H. K., & Zschörner, H. (1961). An annual and a semiannual variation of the upper air density. *Geofisica pura e applicata*, *48*(1), 85–92. https://doi.org/10.1007/BF01992371

Qian, L., Burns, A. G., Emery, B. A., Foster, B., Lu, G., Maute, A., & Wang, W. (2013). The NCAR TIE-GCM: A community model of the coupled thermosphere/ionosphere system. In *Modeling the ionosphere–thermosphere system* (Vol. 201, pp. 73–83). American Geophysical Union (AGU). https://doi.org/10.1002/9781118704417.ch7

Qian, L., & Solomon, S. C. (2012). Thermospheric density: An overview of temporal and spatial variations. *Space Science Reviews*, *168*(1–4), 147–173. https://doi.org/10.1007/s11214-011-9810-z

Qian, L., Solomon, S. C., & Kane, T. J. (2009). Seasonal variation of thermospheric density and composition. *Journal of Geophysical Research*, *114*(A1), 2008JA013643. https://doi.org/10.1029/2008JA013643

Qian, L., Yu, W., Pedatella, N., Yue, J., & Wang, W. (2023). Hemispheric asymmetry of the annual and semiannual variation of thermospheric composition. *Journal of Geophysical Research: Space Physics*, *128*(5), e2022JA031077. https://doi.org/10.1029/2022JA031077

Russell, C. T., & McPherron, R. L. (1973). Semiannual variation of geomagnetic activity. *Journal of Geophysical Research*, *78*(1), 92–108. https://doi.org/10.1029/JA078i001p00092

Schieldge, J., & Siscoe, G. (1970). A correlation of the occurrence of simultaneous sudden magnetospheric compressions and geomagnetic bay onsets with selected geophysical indices. *Journal of Atmospheric and Terrestrial Physics*, *32*(11), 1819–1830. https://doi.org/10.1016/0021-9169(70)90139-X

Scolini, C., Messerotti, M., Poedts, S., & Rodriguez, L. (2018). Halo coronal mass ejections during Solar Cycle 24: Reconstruction of the global scenario and geoeffectiveness. *Journal of Space Weather and Space Climate*, *8*, A09. https://doi.org/10.1051/swsc/2017046

Siemes, C., De Teixeira Da Encarnação, J., Doornbos, E., Van Den IJssel, J., Kraus, J., Pereštý, R., et al. (2016). Swarm accelerometer data processing from raw accelerations to thermospheric neutral densities. *Earth Planets and Space*, *68*(1), 92. https://doi.org/10.1186/s40623-016-0474-5

Solomon, S. C., & Qian, L. (2005). Solar extreme-ultraviolet irradiance for general circulation models. *Journal of Geophysical Research*, *110*(A10), A10306. https://doi.org/10.1029/2005JA011160

Sutton, E. K., Forbes, J. M., & Nerem, R. S. (2005). Global thermospheric neutral density and wind response to the severe 2003 geomagnetic storms from CHAMP accelerometer data. *Journal of Geophysical Research*, *110*(A9), 2004JA010985. https://doi.org/10.1029/2004JA010985

Torr, M. R., Richards, P. G., & Torr, D. G. (1980). A new determination of the ultraviolet heating efficiency of the thermosphere. *Journal of Geophysical Research*, *85*(A12), 6819–6826. (origin of the heating efficiency concept). https://doi.org/10.1029/JA085iA12p06819

Vasyliunas, V. M., Kan, J. R., Siscoe, G. L., & Akasofu, S.-I. (1982). Scaling relations governing magnetospheric energy transfer. *Planetary and Space Science*, *30*(4), 359–365. https://doi.org/10.1016/0032-0633(82)90041-1

Volland, H., & Mayr, H. G. (1971). Response of the thermospheric density to auroral heating during geomagnetic disturbances. *Journal of Geophysical Research*, *76*(16), 3764–3776. https://doi.org/10.1029/JA076i016p03764

Wang, X., Miao, J., Aa, E., Ren, T., Wang, Y., Liu, J., & Liu, S. (2020). Statistical analysis of joule heating and thermosphere response during geomagnetic storms of different magnitudes. *Journal of Geophysical Research: Space Physics*, *125*(8), e2020JA027966. https://doi.org/10.1029/2020JA027966

Wang, X., Miao, J., Lu, X., Aa, E., Liu, J., Wang, Y., & Liu, S. (2021). Latitudinal impacts of joule heating on the high-latitude thermospheric density enhancement during geomagnetic storms. *Journal of Geophysical Research: Space Physics*, *126*(7), e2020JA028747. https://doi.org/10.1029/2020JA028747

Webb, D. F., & Howard, R. A. (1994). The solar cycle variation of coronal mass ejections and the solar wind mass flux. *Journal of Geophysical Research*, *99*(A3), 4201–4220. https://doi.org/10.1029/93JA02742

Weimer, D. R. (2005). Improved ionospheric electrodynamic models and application to calculating Joule heating rates. *Journal of Geophysical Research*, *110*(A5), 2004JA010884. https://doi.org/10.1029/2004JA010884

Wilson, G. R., Weimer, D. R., Wise, J. O., & Marcos, F. A. (2006). Response of the thermosphere to Joule heating and particle precipitation. *Journal of Geophysical Research*, *111*(A10), 2005JA011274. https://doi.org/10.1029/2005JA011274

Woods, T. N., Eparvier, F. G., Hock, R., Jones, A. R., Woodraska, D., Judge, D., et al. (2012). Extreme ultraviolet variability experiment (EVE) on the solar dynamics observatory (SDO): Overview of science objectives, instrument design, data products, and model developments. *Solar Physics*, *275*(1), 115–143. https://doi.org/10.1007/s11207-009-9487-6

Xiong, C., Lühr, H., Schmidt, M., Bloßfeld, M., & Rudenko, S. (2018). An empirical model of the thermospheric mass density derived from CHAMP satellite. *Annales Geophysicae*, *36*(4), 1141–1152. https://doi.org/10.5194/angeo-36-1141-2018

Yiğit, E., Medvedev, A. S., & Ern, M. (2021). Effects of latitude-dependent gravity wave source variations on the middle and upper atmosphere. *Frontiers in Astronomy and Space Sciences*, *7*, 614018. https://doi.org/10.3389/fspas.2020.614018

Yue, C., Zong, Q. G., Zhang, H., Wang, Y. F., Yuan, C. J., Pu, Z. Y., et al. (2010). Geomagnetic activity triggered by interplanetary shocks. *Journal of Geophysical Research*, *115*(A5), 2010JA015356. https://doi.org/10.1029/2010JA015356

Yue, J., Jian, Y., Wang, W., Meier, R. R., Burns, A., Qian, L., et al. (2019). Annual and semiannual oscillations of thermospheric composition in TIMED/GUVI limb measurements. *Journal of Geophysical Research: Space Physics*, *124*(4), 3067–3082. https://doi.org/10.1029/2019JA026544

Zhao, H., & Zong, Q. (2012). Seasonal and diurnal variation of geomagnetic activity: Russell-McPherron effect during different IMF polarity and/or extreme solar wind conditions. *Journal of Geophysical Research*, *117*(A11), 2012JA017845. https://doi.org/10.1029/2012JA017845